Wide Bandgap Semiconductor Based High Performance Bidirectional CLLL Converter for Electric Vehicle Application

by

Md. Tanvir Shahed

Roll: 0419062133

MASTER OF SCIENCE

IN

ELECTRICAL AND ELECTRONIC ENGINEERING

Department of Electrical and Electronic Engineering

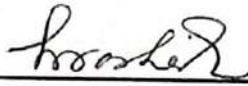Bangladesh University of Engineering and Technology

Dhaka, Bangladesh

April, 2023

Approval

This thesis titled, **"Wide Bandgap Semiconductor Based High Performance Bidirectional CLLL Converter for Electric Vehicle Application"**, submitted by Md. Tanvir Shahed, Roll No.: 0419062133, Session: April 2019, has been accepted as satisfactory in partial fulfillment of the requirement for the degree of MASTER OF SCIENCE in Electrical and Electronic Engineering on 16th April, 2023.

BOARD OF EXAMINERS

Dr. A.B.M. Harun-ur-Rashid
Professor
Department of EEE, BUET, Dhaka
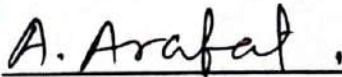
Chairman
(Supervisor)

Dr. Md. Aynal Haque
Professor and Head
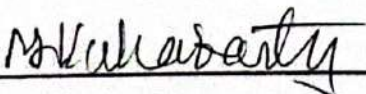Department of EEE, BUET, Dhaka

Member
(Ex-Officio)

Dr. Md. Ziaur Rahman Khan
Professor
Department of EEE, BUET, Dhaka

Member

Dr. Muhammad Abdullah Arafat
Assistant Professor
Department of EEE, BUET, Dhaka

Member

Dr. Tapan Kumar Chakraborty
Professor
Department of EEE, University of Asia Pacific, Dhaka

Member
(External)

Declaration

This is to certify that the work presented in this thesis entitled, "Wide Bandgap Semiconductor Based High Performance Bidirectional CLLL Converter for Electric Vehicle Application", is the outcome of the research carried out by Md. Tanvir Shahed under the supervision of Dr. A.B.M. Harun-ur Rashid, Professor, Department of Electrical and Electronic Engineering (EEE), Bangladesh University of Engineering and Technology (BUET), Dhaka-1000, Bangladesh.

It is also declared that neither this thesis nor any part thereof has been submitted anywhere else for the award of any degree, diploma, or other qualifications.

Signature of the Candidate

Md. Tanvir Shahed
Roll No: 0419062133

Dedication

To my beloved family

Contents

List of Figures

List of Tables

x

List of Acronyms

2DEG   2D Electron Gas

AAV   Autonomous Aerial Vehicle
AC   Alternating Current
ADRC   Active Disturbance Rejection Controller

BCS   Battery Charging Station
BDC   Bidirectional DC-DC converter
BESS   Battery Energy Storage System
BEV   Battery Electric Vehicle
BMS   Battery Management System

CM   Common-Mode
CP   Charging Post
CPL   Constant Power Load
CPM   Charging Post Manager
CPT   Capacitive Power Transfer

DAB   Dual Active Bridge
DB   Depleted Battery
DC   Direct Current
DDPG   Deep Deterministic Policy Gradient
DNN   Deep Neural Network
DQN   Deep Q Network
DRL   Deep Reinforcement Learning
DSO   Distribution System Operator
DVR   Double Voltage Rectification

EMF   Electromagnetic Field
EMI   Electromagnetic Interference

ER-EV	Extended-Range Electric Vehicle
EV	Electric Vehicle
EVSE	Electric Vehicle Supply Equipment
FB	Fully Charged Battery
FCEV	Fuel Cell Electric Vehicle
FET	field-effect transistor
FHA	First Harmonic Approximation
FRD	fast recovery diode
G2V	Grid to Vehicle
GA	Genetic Algorithm
GaN	Gallium Nitride
HEMT	High Electron Mobility Transistor
HEV	Hybrid Electric Vehicle
HF	High Frequency
ICE	Internal Combustion Engine
IEC	International Electrotechnical Commission
IEEE	Institute of Electrical and Electronics Engineers
IGBT	Insulated-Gate Bipolar Transistor
IPT	Inductive Power Transfer
IPTS	Inductive Power Transfer System
IRENA	International Renewable Energy Agency
ITAE	Integral of Time Weighted Absolute Error
MEA	More Electric Aircraft
MOSFET	Metal-Oxide-Semiconductor Field-Effect Transistor
NACS	North American Charging Standard
PFC	Power Factor Correction
PHEV	Plug-In Hybrid Electric Vehicle

PID	Proportional-Integral-Derivative
PSO	Particle Swarm Optimization
PWM	Pulse Width Modulation
RCD	Residual Current Device
RES	Renewable Energy Sources
SAC	Standards Administration of China
SAE	Society of Automotive Engineers
Si	Silicon
SiC	Silicon Carbide
SUV	Sports Utility Vehicle
TD3	Twin Delayed Deep Deterministic Policy Gradient
TSO	Transmission System Operator
UPS	Uninterruptible Power Supplies
V2G	Vehicle to Grid
WBG	Wide Bandgap
WPT	Wireless Power Transfer
ZCS	Zero Current Switching
ZOH	Zero Order Hold
ZVS	Zero Voltage Switching

Acknowledgement

Abstract

This thesis proposes an improved topology for an isolated bidirectional resonant dc-dc converter for electric vehicle (EV) onboard chargers. As opposed to the conventional capacitor-inductor-inductor-inductor-capacitor (CLLLC) resonant converter, the proposed converter's resonant circuit is composed of a capacitor-inductor-inductor-inductor (CLLL) structure, whose inductances, except the capacitor, can be fully integrated with the leakage and mutual inductances of the high-frequency (HF) transformer. Therefore, this offers a smaller size, lower costs, minimal power loss, and eventually higher efficiency. Again, the proposed converter design is based on wide bandgap (WBG) transistor switches that operate at MHz-level switching frequency to achieve high power density, high efficiency, and high compactness. To assure closed-loop control of the proposed CLLL converter, a discrete-time proportional integral derivative (PID) controller has first been designed using the phase-shifted pulse width modulation (PSPWM) method. The genetic algorithm (GA) and particle swarm optimization (PSO) algorithms have both been used to optimize the PID controller parameters and a comparison between the two algorithms have been provided. Second, an intelligent controller based on deep reinforcement learning (DRL) has been proposed to automate the controller process. A comparison of the DRL and PID controllers has also been provided, and the DRL controller performed better than the conventional PID controller. To achieve fast switching with very little switching loss, the converter is simulated with several Wide Bandgap (WBG) switching devices. A performance comparison with conventional Si-based switching devices is also provided. An accurate power loss model of the switching devices has been developed from the manufacturer's datasheet to achieve the perfect thermal design of the converter. A $5\,kW$ CLLL converter with an input range of $400 - 460\,V$ direct current (DC) and an output range of $530 - 610\,V$ DC and a switching frequency of 1 MHz has been designed and investigated under various loading scenarios. Gallium Nitride (GaN) switching device-based designs achieved the highest levels of efficiency among the switching devices. The efficiency of this device is 97.40 percent in forward mode and 96.67 percent in reverse mode.

Chapter 1

Introduction

This chapter describes the rationale behind the quest for high-performance, isolated bidirectional resonant converters for use in onboard chargers for electric vehicles (EVs) and covers some of the strategies and techniques used by researchers to improve the performance of currently available resonant converters. Lastly, the objective and outline of the thesis will be explained.

1.1 Electric Vehicles

Electric vehicles (EVs), an eco-friendly automotive alternative, are growing quickly in popularity worldwide. Countries all over the world are promoting this initiative through a variety of strategies, including tax incentives, VAT exemption, decreased license tax, purchase aids, toll exemption, free public parking, etc. The adoption of EVs over conventional internal combustion engine (ICE) vehicles has been accelerated for a variety of reasons. These are:

- Fossil Fuel Depletion: Fossil fuel reserves are running out globally. As a result, there is a shortage of fossil fuels. The cost of fossil fuels is also significantly rising.

- Zero Emission: Unlike conventional ICE vehicles, EVs don't produce any air pollutants like carbon dioxide (CO_2), nitrogen oxides (NO_x), carbon monoxide (CO), sulfur dioxide (SO_2), or particulate matter (PM), etc.

- Advances in Supporting Technology: Grid-to-Vehicle (G2V) and Vehicle-to-Grid (V2G) systems, as well as renewable energy technologies, assisted in the

growth of EVs. The rapid growth of EVs was aided by the development of EV charging technologies and electronic control systems for EV propulsion.

All of these factors have contributed to a significant increase in the number of global EV sales, particularly in the previous two years, as shown in Figure 1.1 and Figure 1.2 [1].
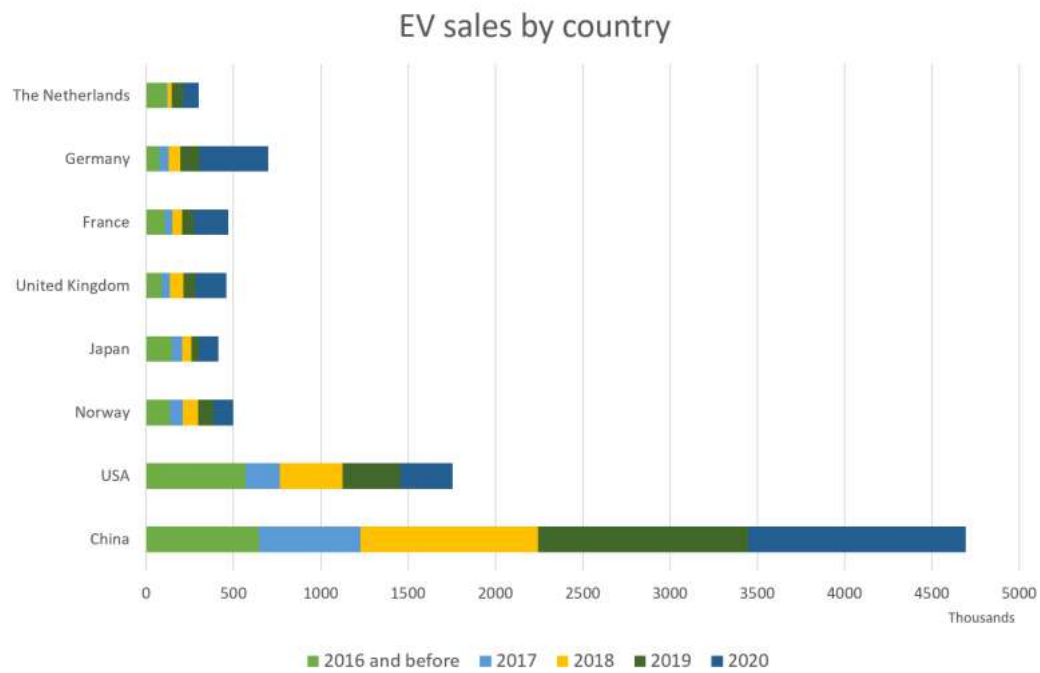
Figure 1.1: Changes in the global sales of electric vehicles [1].
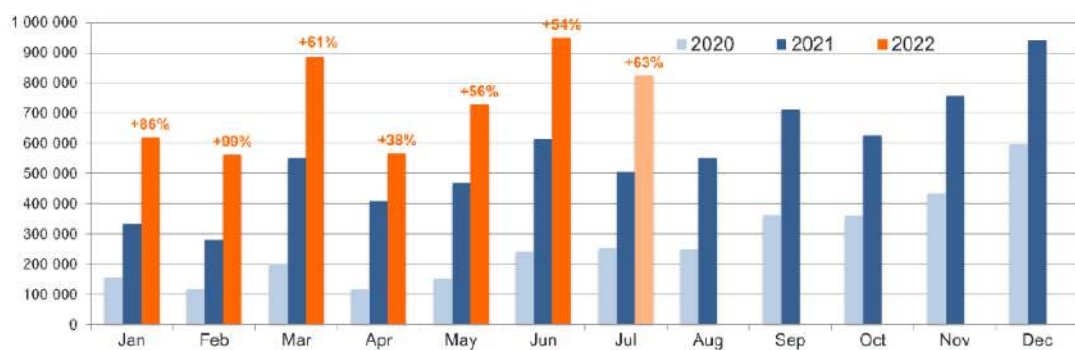
Figure 1.2: Global monthly plug-in EV sales and year-to-year growth [1].

1.2 Electric Vehicles Types

We can categorize EVs into five different types based on their engine technology. Following is a brief overview of these types:

- Battery Electric Vehicles (BEVs): This is a fully electric vehicle that is powered entirely by electricity. It can move without using any ICE or liquid fuel. BEVs are consequently better for reducing global warming and climate change. Large battery packs are used to power the vehicle. Regenerative braking is a feature of BEVs that converts kinetic energy back into electrical energy that can be retained by the battery. Consequently, EVs are preferable for city driving since city driving frequently involves starting and stopping, which causes the vehicle to recover part of the kinetic energy into the battery. Figure 1.3 depicts the structure and essential elements of a BEV [2]. A typical BEV can go 95 to 695 kilometers on a single charge. The Ford Mustang Mach-E, a BEV compact crossover Sports Utility Vehicle (SUV) manufactured by Ford in December 2020, is an instance of this kind of vehicle. It presently offers a 68-88 kWh battery that allows consumers to have an autonomy of 370-483 km. The vehicle was named the 2021 North American SUV of the Year.
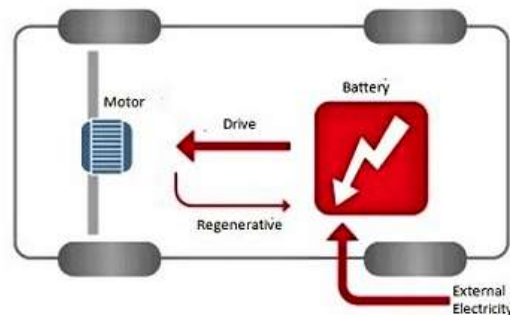
Figure 1.3: The structure and key elements of a BEV [2].

- Plug-In Hybrid Electric Vehicles (PHEVs): A traditional internal combustion engine and an electric motor, powered by an external electric source that can be plugged in, work together to drive plug-in hybrid automobiles. PHEVs have the capacity to store enough grid power to dramatically lower their fuel use under normal driving circumstances. They have regenerative braking, just like BEVs. The structure and key components of a PHEV are shown in Figure 1.4 [2]. The 8.8 kWh battery in the Toyota Prius PHEV enables it to go around 40 km on its electric powertrain alone. It has an

average driving range of 1030 kilometers. It is also important to note that PHEVs use more gasoline than car manufacturers claim.
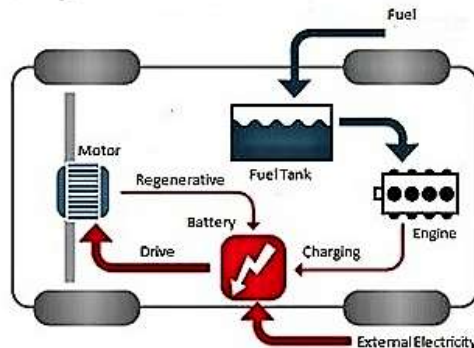
Figure 1.4: The structure and key components of a PHEV [2].

- Hybrid Electric Vehicles (HEVs): HEVs use both an electric motor and a gas engine to propel the vehicle. Regenerative braking, which recovers energy normally lost during braking to support the gasoline engine during acceleration, provides all of the energy for the batteries. This braking energy often escapes from a standard ICE car as heat in the brake pads and rotors. Regular hybrids cannot use the grid to recharge, in contrast to PHEVs. Figure 1.5 illustrates an HEV's structure and key components [2]. If one can afford the higher price tag, HEVs are a no-brainer because we don't have to worry about finding charging stations or spending extra time powering up. They are often more expensive than gas-powered automobiles by a few thousand dollars, but less expensive than PHEVs. For instance, the base price of a gas-powered Toyota Rav 4 in 2022 is $26,975. The cost of the same car HEV model is $29,575 while the PHEV model is $40,300. However, it is simple to see how the expense eventually balances out whenever gas prices increase.
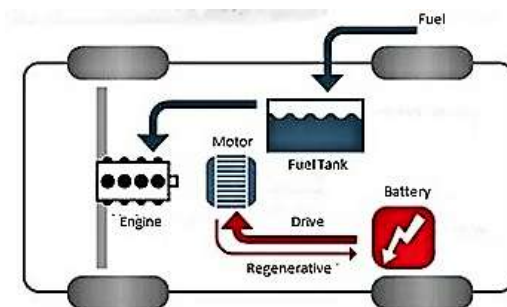
Figure 1.5: The structure and essential elements of a HEV [2].

- Fuel Cell Electric Vehicles (FCEVs): These cars are equipped with an electric motor that burns a combination of compressed hydrogen and oxygen that is taken from the air, with water being the sole waste product. Despite the fact that these vehicles are regarded as having "zero emissions," it is important to note that while there is green hydrogen, the majority of the hydrogen consumed is produced from natural gas. Figure 1.6 shows an FCEV's basic components and structural layout [2]. An example of one of these cars is the Toyota Mirai, whose most recent model was introduced in 2021 and has a range of 650 kilometers without refueling and produces only clean water as emissions.
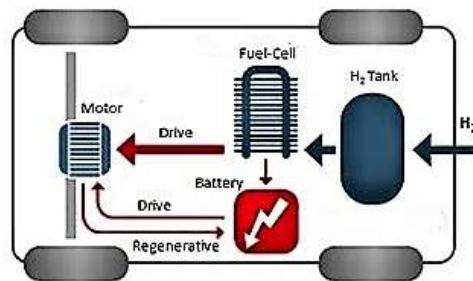
Figure 1.6: The structural layout and basic elements of an FCEV [2].

- Extended-Range EVs (ER-EVs): A range extender is an additional power source that extends the driving range of an extended-range electric vehicle (ER-EV). The majority of range extenders use tiny internal combustion engines to power an electric generator, which supplies power to the motor and electric batteries. When an ER-EV's tiny range-extender motor is running, CO_2 is produced, but not when the ER-EV is using electric power. An ER-EV will emit much less CO_2 than an ICE vehicle over the course of its lifespan. Figure 1.7 illustrates an ER-EV's structure and key components [3]. The BMW i3 is an instance of an ER-EV. It has a lithium-ion battery pack and an optional range-extending gasoline engine.

1.3 G2V and V2G Technology

Grid-to-vehicle power or energy flows are referred to as "G2V" or "charging mode," while vehicle-to-power or energy flows are referred to as "V2G" or "discharging mode." Figure 1.8 shows a V2G framework that has interactions among power sys-
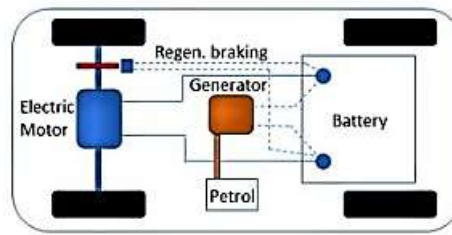
Figure 1.7: The structure and essential elements of an ER-EV [3].

tem operators, consumers, and EV users [4]. Here, these V2G systems can work in a G2V mode. Traditional generators, RESs, and transmission infrastructure are included in the power systems. Both customers (such as household, commercial, and industrial users) and V2G systems are supplied with energy by the power systems. The V2G networks are made up of EVs that are connected to the power grid through aggregators and public and private charging stations. A mediator who controls and optimizes energy flow between the power grid and V2G systems is known as an aggregator. It functions as energy storage in V2G mode and as a consumer in G2V mode. V2G communication, which consists of communications networks like wireless networks and processing capabilities like data centers and cloud computing, enables data and information interchange between power systems, electricity consumers, and V2G systems. The power system operators can efficiently optimize power generation and auxiliary services from EVs thanks to the V2G communications networks, which allow them to get the data they need from V2G systems and electricity users.

1.3.1 Smart G2V or V2G Systems

Fast charging or G2V infrastructure is expanding globally as a result of the rapid expansion of EVs. When an EV is attached to a charger, the EV battery will either begin charging instantly or after a wait. If most EVs charge at the same time, there will be a high demand for power and energy from the power grid, which will lead to an undesirable low voltage within the distribution network. The term "uncoordinated charging" or "uncontrolled charging" is frequently used to describe this circumstance. Such a condition could negatively impact the distribution grid by increasing actual power losses, violating voltage limitations, and overloading distribution network assets such as transformers and cables/lines. The lifespan of distribution transformers will eventually be shortened. It will lead to network congestion and reliability issues for the transmission grid. And it will cause problems for the generation grid including an increase in unit pricing, capacity expansion,
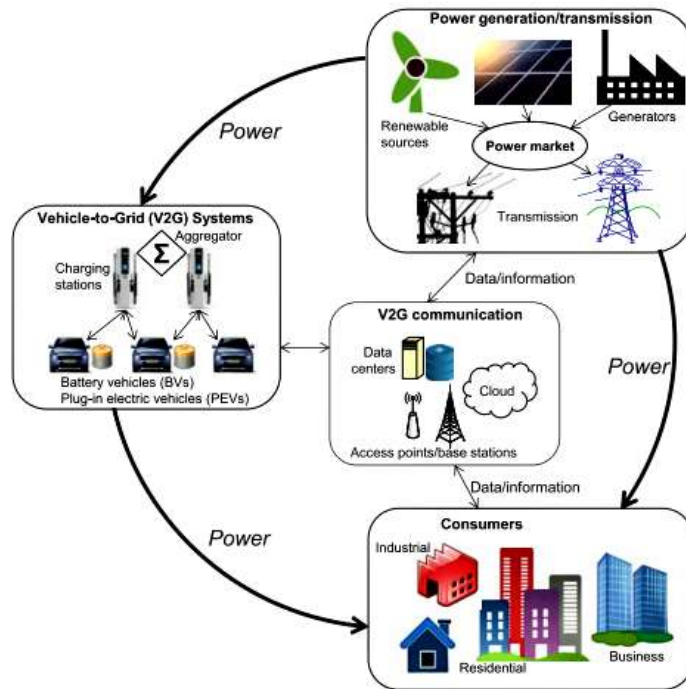
Figure 1.8: A V2G framework [4].

and higher use of generation assets. Unmanaged vehicle-to-grid (V2G) networks might have similar effects. By managing the charging in a planned manner, smart charging can address these problems. By implementing dynamic pricing regulations, coordinated smart charging could save charging costs while enhancing the functioning of the power grid. The advantages of smart charging may be passed on to individual consumers in two ways: directly by lowering their charging prices and indirectly by decreasing distribution grid losses, distribution network capital costs, transformer life loss, valley filling (timed mechanisms to drain electricity while grid demand is low), and peak shaving (lowering the grid's peak electricity demand). In order to successfully integrate EVs and renewable energy sources (RES) into the grids in the future, the International Renewable Energy Agency (IRENA) thinks that smart charging and consumer subsidies have become two crucial aspects.

Smart charging and discharging control systems are divided into two categories: centralized and decentralized approaches. With centralized approaches, an authorized energy service provider known as an aggregator is in charge of all EV charging and discharging operations through CPs (charging posts) or CPMs (charging post managers). If DSO (Distribution System Operator) requests a load reduction or increase, the aggregator will carry out the power purchase directly in the

day-ahead electricity market after receiving TSO (Transmission System Operator) approval. If the TSO requests ancillary services like secondary and tertiary frequency regulation, the aggregator can also engage in the ancillary services market in addition to the day-ahead market. The centralized control framework for EVs is shown in Figure 1.9 [5]. In contrast, choices regarding charging and discharging are made and carried out by EVs themselves in decentralized approaches. Figure 1.10 demonstrates the decentralized control framework used by EVs [5]. Even though the centralized strategy can achieve the best outcomes for both the provider and the EVs, it might not be feasible to execute since with this approach the EVs are unable to independently regulate their charging and discharging processes. Due to user acceptability and reduced communication, the decentralized method is therefore preferred in real systems.
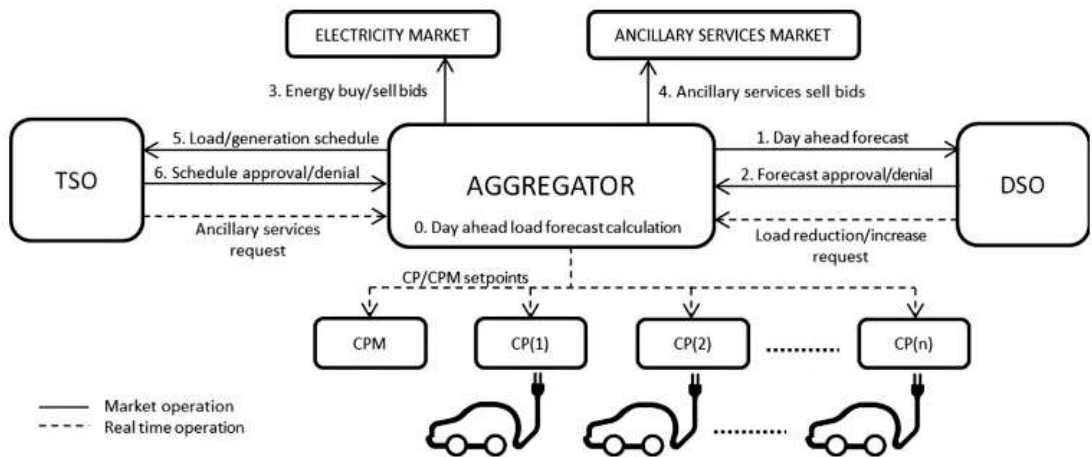
Figure 1.9: A centralized control framework for EVs [5].
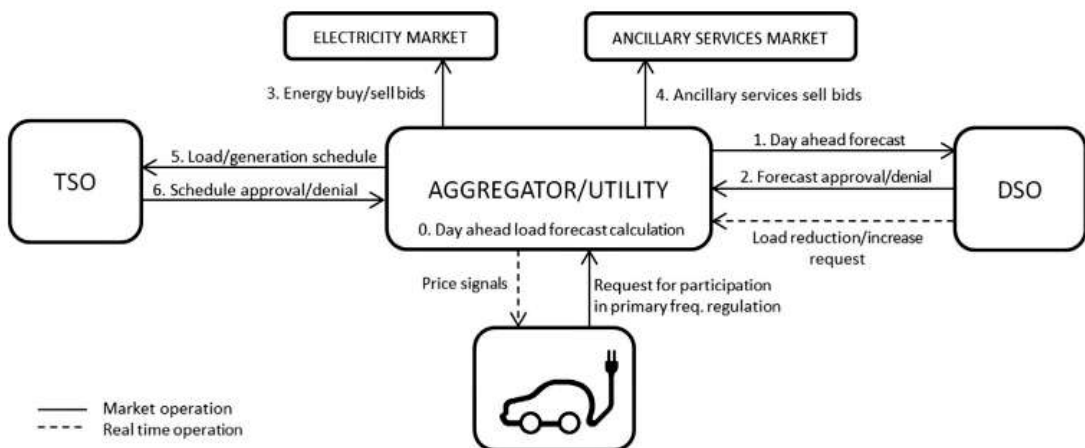
Figure 1.10: A decentralized control framework for EVs [5].

1.3.2   V2G Systems Benefits

Smart V2G of EVs can enhance the efficiency, reliability, and stability of the power grid. Additionally, they benefit EV users economically. The following are some advantages of V2G technology:

- Ancillary Services: EVs are viewed as dynamic distributed energy sources in this V2G that assist the electrical grid. This is conceivable since EVs are projected to be parked 96% of the time. They are able to offer ancillary services like spinning reserves, voltage regulation, and frequency regulation. A smart V2G of EV can provide active power regulation, load balancing, harmonic filtering, inertia support, reactive power support, and the best possible use of variable RESs. As a result, system administrators would be able to manage the power system safely with lower synchronous generation.

- Improved Quality of Service: Modern battery technology allows smart V2G systems to instantly return energy to the grid. As a result of the V2G system's quick response, system operators can provide consumers with better power quality.

- Storage Solution for Renewable Energy Integration: By utilizing EVs as storage devices, the power quality from RESs like solar and wind energy can be significantly enhanced. The power grid can be made more reliable and stable by combining EVs and RESs.

- Increased Revenue for EV Users: In exchange for joining the V2G system, EV users can get payment from the V2G operators for the energy they discharge. Therefore, EV customers might balance their needs and charging/discharging operations by using intelligent energy management solutions, such as charging during off-peak hours and discharging throughout peak hours, to increase earnings.

- Reduced Environmental Pollution: EVs, as opposed to traditional vehicles that use fossil fuels, can dramatically reduce environmental pollution, even when power-generating emissions are taken into account. According to estimates, emissions of CO_2 can be reduced by 2.2 tons annually by switching from a traditional vehicle to an EV.

However, there are still a number of difficulties that V2G must overcome, including early battery deterioration, investments in communications networks to enable

interactions between EVs and the grids, protection against cyber-attacks, impacts on grid equipment, additional infrastructure modifications, and social, cultural, political, and technological barriers. Even though V2G operations can shorten the life of battery packs, it is anticipated to provide financial advantages for both EV owners and system operators.

1.4 Literature Review

Bidirectional DC-DC converters (BDCs) are an essential part of these EVs. They are also used in a wide range of applications that require bidirectional power transmissions, such as renewable energy systems, industrial systems, DC power distribution systems, aerospace power supplies, more electric aircraft (MEA) power supplies, uninterruptible power supplies (UPS), fuel cell and battery energy storage systems (BESS). This type of high-power bidirectional DC-DC resonant converter is capable of achieving both DC voltage variation and electrical isolation. Figure 1.11 depicts a block diagram of a standard EV onboard charger, which includes an AC-DC PFC (Power Factor Correction) stage and a bidirectional DC-DC converter. The PFC stage is connected to the AC grid and a DC link capacitor to achieve unity PFC and AC-to-DC conversion. The bidirectional DC-DC converter connects the DC link capacitor and an EV battery pack to achieve current and voltage regulation as well as galvanic isolation. These bidirectional dc-dc converters can power EV battery loads while also providing power feedback to the power grid. Dual active bridge (DAB) [6], and CLLLC [7] converters are among the current bidirectional DC-DC converter topologies that have drawn a lot of focus because of the high-frequency (HF) transformers' simplistic and symmetrical architecture on both sides. The main benefit of DAB architecture over a CLLLC resonant converter is the lack of resonant capacitors that need to withstand high voltage stresses. Contrarily, the CLLLC resonant converter has the ability to soft-switch in almost any loading situation. These converter switches can achieve zero voltage switching (ZVS) on the inverter side as well as zero current switching (ZCS) on the rectification side without the need for an auxiliary circuit, enabling them to work at higher switching frequencies.

Several research studies have been carried out to improve the performance of CLLLC converters for a variety of applications because of the CLLLC converter's current popularity and its broad application prospects. For instance, in [8], an innovative operation mode analysis was developed to determine the optimum tank
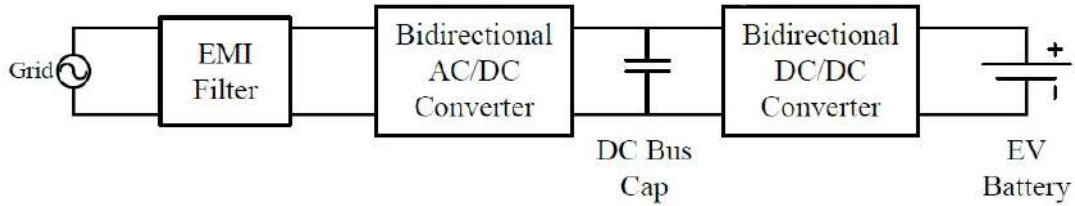
Figure 1.11: Block schematic of a typical EV onboard charger.

parameters for a specific set of circumstances. To build high-power-density res-
onant converters, it is shown in [9] that increasing the switching frequency from
65 kHz to 1 MHz reduces the overall size of capacitors and inductors by almost
half. Zong et al. [10] developed a double voltage rectification (DVR) modulation
technique that provides a step-up voltage gain to widen the operating voltage
range of bidirectional resonant converters. A technique to lessen electromagnetic
interference (EMI) noise caused by common-mode (CM) CLLLC converters was
put forth by Chu et al. [11]. As a result, CM chokes can be reduced in size,
while the converter power density can be increased. However, in symmetrical
bidirectional topologies, such as the CLLLC converter [7], there are at least five
resonant elements, whereas, in asymmetric bidirectional topologies, such as the
proposed CLLL converter, there will be only four resonant elements, reducing the
difficulty of parameter design. It also minimizes the design's size and cost. This
proposed CLLL resonant network combines all of the advantages of a lower-order
resonant converter, absorbing all parasitic components and enabling operation at
high switching frequencies with minimal switching losses. The resonant inductors
can be synthesized from the HF transformer's leakage inductance and fully inte-
grated with the HF transformer. By altering the air gap between the windings
and core halves, the leakage inductance can be changed. The loss and core vol-
ume of the converter will be reduced as a result of this integrated transformer.
As a result, asymmetric bidirectional topologies are thought to be more flexible
and efficient. However, no breakthroughs in the field of asymmetric bidirectional
topologies research have been made since it is challenging to develop a parameter
design procedure that equips the converter with a similar bidirectional operating
characteristic.

Furthermore, passive storage components account for a sizable portion of the to-
tal size of switching converters. Passive storage components make up a significant
portion of the overall size of switching converters. The most obvious method
for lowering the size of magnetic components is unquestionably the use of higher

switching frequencies. Nonetheless, even partial hard-switching at a higher switching frequency at any switching device could cause significant switching losses, degrading efficiency noticeably and adding to the burden of thermal management. Because of this, this paper, which focuses on EV onboard charger application areas, uses the CLLL resonant structure as a more practical choice for HF DC-DC conversion without no extra control complexity needed to enable soft switching.

Additionally, as semiconductor technology develops, third-generation wide-bandgap semiconductor devices like silicon carbide (SiC) and gallium nitride (GaN) devices have been developed to help bidirectional converters achieve relatively high switching frequency, high power density, and high efficiency by displacing conventional devices like silicon MOSFETs and silicon IGBTs. An overall view of a few key material characteristics of these devices is given in [12]. GaN material is a great option for high-voltage and high-frequency applications because it has the highest breakdown voltage, bandgap, and electron velocity characteristics, according to the comparative data presented in [12]. Despite having less thermal conductivity than SiC, GaN devices can offer high power densities with efficient cooling techniques. Additionally, GaN devices feature lower gate charges and on-resistance than Si and SiC devices, resulting in lower switching charges and rapid switching transitions. Furthermore, rapid switching transitions lead to less switching loss. Besides that, GaN has a lesser output capacitance, which results in reduced switching loss and makes it simpler to implement ZVS. Other Si and SiC-based devices require an anti-parallel diode, but GaN 2D Electron Gas (2DEG) does not require one because it can conduct in the third quadrant. It consequently has no reverse recovery loss, which lowers switching loss and reduces EMI noise. GaN FETs are therefore capable of maintaining high efficiency during the high-frequency operation among the switching devices that are currently available.

1.5 Objectives of the Thesis

In this context, the following are the objectives of this work:

I. To design a high-performance bidirectional asymmetric CLLL resonant dc-dc converter for EV charging (G2V) or discharging (V2G) applications with a high voltage gain.

II. To choose an effective switching device for the design by testing the designed converter with various switching device models from various manufacturers.

III. To examine how various design factors affect the proposed converter's performance and improve the system's charging and discharging efficiency.

IV. To develop a PID controller based on the PSPWM technique, and use PSO, and GA optimization algorithms to optimize its parameters.

V. To devise a deep reinforcement learning (DRL)-based intelligent controller to regulate the output voltage and evaluate its performance against the designed PID controller.

1.6 Thesis Outline

The rest of this thesis is organized as follows.

Chapter 1 begins with a general introduction to EVs and their various types, followed by the significance of V2G and G2V technology, a problem statement, and the objectives of this work.

Chapter 2 provides a brief summary of current battery charging methods as well as past work done by researchers on various types of BDCs, which serves as the thesis's cornerstone. Additionally, it discusses how the proposed converter operates.

Chapter 3 describes the design, numerical methodologies, and simulation approach used to generate the performance measurements. It also contains the controller's in-depth design and analysis.

Chapter 4 contains simulation results, a discussion, and a performance study of the proposed converter in contrast to existing BDC designs.

Chapter 5 includes the concluding remarks as well as recommendations for future work on this proposed converter.

Chapter 2

Overview of EV Battery Charging

This chapter provides a brief overview of the theoretical concepts involved in this work. The first part of the article reviews the most recent advancements in EV charging and discharging technologies. A brief overview of the current BDC converters developed by the researchers is provided in the chapter's later sections. Additionally, it briefly outlines the researchers' efforts to enhance the performance of this type of converter.

2.1 EV Charging Technologies and Standards

This section provides a brief explanation of the various EV charging configurations, including on-board and off-board, charging stations, charging standards like IEC (International Electrotechnical Commission) and SAE (Society of Automotive Engineers), and country-specific EV charging stations and connectors.

2.1.1 EV Charging Standards

To handle EV charging infrastructure, various governing bodies have created uniform charging standards. Different countries use different charging standards. For instance, Japan and Europe utilize CHAdeMO as their charging standard, while the United States prefers the Institute of Electrical and Electronics Engineers (IEEE) and SAE standards. The Standards Administration of China (SAC) employs IEC-compliant GB/T standards. The word "Level" is used to describe the power rating in SAE, whereas "Mode" is used in IEC. Table 2.1 provides a summary of the IEC and SAE charging standards.

Table 2.1: Summary of EV charging standards

Standards	Source	Phase	Level/Mode	Voltage (V)	Current (A)
SAE-J1772	AC	Single	Level 1	120	16
		Single	Level 2	240	32-80
	DC	DC	Level 1	200-450	80
		DC	Level 2	200-450	200
IEC-62196	AC	Single	Mode 1	120	16
		Single	Mode 2	240	32
		Single	Mode 3	250	32-250
	DC	DC	Mode 4	600	400
IEC-61851-1	AC, non-dedicated	Single	Mode 1	250	16
		Three		480	16
	AC, non-dedicated	Single	Mode 2	250	32
		Three		480	32
	AC, dedicated	Single	Mode 3	250	32
		Three		480	32
	DC, dedicated	DC	Mode 4	400	200
Tesla-NACS	AC/DC	Single, Three & DC	Compatible to IEC-62196 & IEC-61851-1	500/1000	Up to the manufacturer

According to the SAE-J1772 Standard, AC level 1 and level 2 onboard chargers have been created for power supplies of 120 V and 240 V AC, and are able to produce 1.9 kW and 19.2 kW, respectively. Due to their low power consumption, these onboard chargers are perfect for charging throughout the day. Offboard chargers with a power supply between 200 and 450 volts are designed to use a DC fast charger with an optimal capacity of 50 kW and, most recently, up to 350 kW. The IEC-62196 Standard contains three AC levels and one DC level. It lists four distinct couplers for dc fast charger systems, including Configuration AA (CHAdeMO Association), Configuration BB (also called GB/T and applicable in China), Configuration CC (Type 1 combined charging system, accepted in North America), and Configuration FF (Type 2, integrated charging system, adopted in Europe and Australia). The IEC-61851 Standard uses two AC levels with voltage levels of 120V and 240V and one DC level ranging from 200 to 450. The North American Charging Standard (NACS), which is based on the Tesla supercharger, was just released by Tesla Inc. In a small package, it can provide up to 1 MW of DC charging as well as AC charging. This standard is available in 500-volt and 1,000-volt variations.

Different EV charging modes serve various purposes and provide various charging facilities. Following is a brief description of the charging modes:

- Mode 1 (Slow Charging): Figure 2.1 illustrates how an electric vehicle is charged in Mode 1 [13]. The term "Mode 1 Charging Technology" implies charging in homes or workplaces using a straightforward extension wire with no safety. An EV is charged using this method by being plugged into a regular home outlet. It offers a single-phase or three-phase power socket facility with neutral and earth wires and a maximum current intensity of 16

A. Users are not protected from DC-current shock by this charging technique. There is no communication with or control over the vehicle. As a result, it provides the car owner with minimal protection. Because of this, several nations forbid using this mode of charging.

Figure 2.1: Mode 1 EV charging technology [13].

- Mode 2 (Semi-fast Charging): In contrast to Mode 1 charging, Mode 2 charging cables can offer an in-cable RCD (residual-current device), over temperature and over current protection, and protective earth detection. A domestic and industrial cable with built-in shock protection against AC and DC currents is used for charging in mode 2. Figure 2.2 depicts the charging process for an electric vehicle in Mode 2 [13]. This mode is typically placed on portable chargers for EVs. The pricey nature of this charging option is a result of the strict cable requirements. One-phase or three-phase lines with earthing implemented can be used for charging. In single-phase AC applications, the maximum current and voltage ratings are 32 A and 250 V, respectively, and 32 A and 480 V in three-phase AC applications. The EV supply equipment (EVSE) must meet the following criteria before electricity will be sent to the EVs.

    - Adequate earthing protection
    - No fault conditions, such as an over-current or an overheat, etc.
    - EV has been linked and has requested electricity, which can be seen on the pilot data line

This method is subject to different restrictions in the United States, Canada, Switzerland, Denmark, France, Norway, and Italy.

Figure 2.2: Mode 2 EV charging process [13].

- Mode 3 (Fast Charging): Use of a dedicated charging point or a wall-mounted wall box at home is required for mode 3 charging. Both offer AC or DC current shock prevention. In Mode 3, the EV does not require a specific cable for charging because the connecting cable is included with the wall box or charging station. This mode also allows communication between the vehicle and the EVSE device. It controls how much energy is used, keeps track of the charging process, and has an integrated safety system. Figure 2.3 shows how an electric vehicle in Mode 3 is charged [13]. Currently, Mode 3 charging is the favored method for EV charging. It is the only method permitted in Italy for AC automobile charging in public areas. Even if there are no restrictions imposed by law, charging points functioning in mode 3 typically permit charging up to 32 A and 250 V in single-phase AC and up to 32 A and 480 V in three-phase AC.
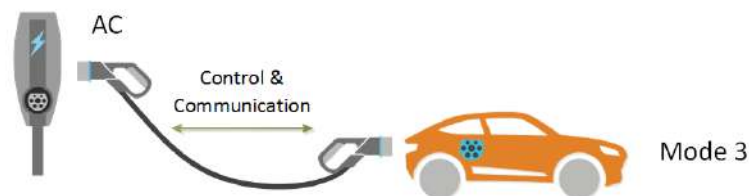
Figure 2.3: EV charging technique for Mode 3 [13].

- Mode 4 (Ultra-fast Charging): The DC charging feature is only available in this charging mode. This charging option needs a current converter that is external to the car where the charging cable is attached. Due to the converter, which converts AC electricity into DC before flowing through the charging cable and toward the electric car, the charging station is often significantly larger than a basic one. With the EVSE, protection, and control features are also available in this mode. Figure 2.4 portrays how to charge an electric vehicle in Mode 4 [13]. This mode offers a maximum charging power capacity of up to 400 kW with a maximum voltage of 1000 V and a current intensity of up to 400 A, in accordance with the most recent IEC-62196-3 standard.

2.1.2 EV Charging Methods

There are three major charging methods for EV charging. They are: conductive charging, inductive charging, and battery swap station (BSS). Compared to inductive charging technology solutions, which are still being researched and are
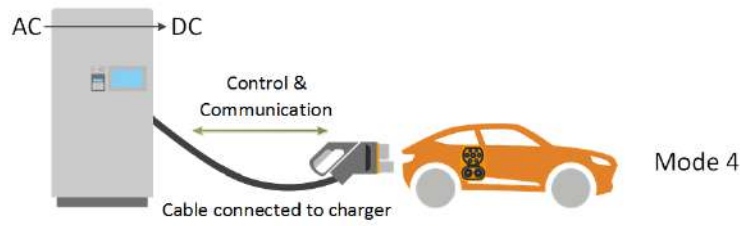
Figure 2.4: EV charging technology for Mode 4 [13].

not yet widely used in the field of electric transportation, conductive charging techniques are more well-established and prevalent. Compared to the other two charging techniques, BSS is less commonly used. Current EV charging methods are depicted in Figure 2.5.
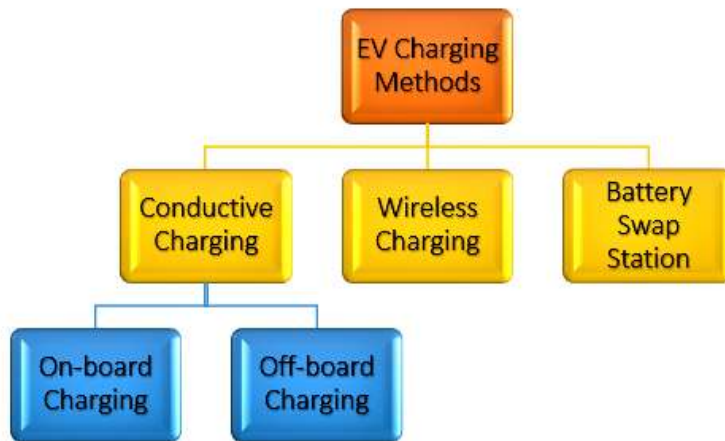
Figure 2.5: A schematic layout of EV charging methods.

2.1.2.1 Conductive Charging

Direct contact between the car and the charging inlet is necessary to transfer power for conductive charging. Because of the direct connection, this charging technique is quite effective. It offers a variety of charging options, including level 1, level 2, level 3 as well as level 4 charging. Conductive charging technology provides a V2G infrastructure, reduces grid losses, maintains system voltage, prevents grid overloading, provides active power, and can even make use of the vehicle's battery to make up for reactive power. Onboard and off-board charging are the two main categories of conductive charging. Off-board charging refers to charging that takes place outside the vehicle, while onboard charging is primarily used for slow charging inside the vehicle. Off-board chargers are preferable because they provide fast charging capabilities, higher kW transfers, and lighter vehicle

weights. The transfer of high power in onboard charging is constrained by weight, size, and cost factors. Because of this, it requires more time to charge than the off-board charging configuration. In contrast to off-board charging, which delivers DC power to the EV battery packs, onboard charging supplies AC power to the batteries. Figure 2.6 depicts the onboard and off-board charging methods [14]. The vehicle's internal battery pack is charged under the control of the battery management system (BMS). The majority of EV manufacturers currently use conductive charging.
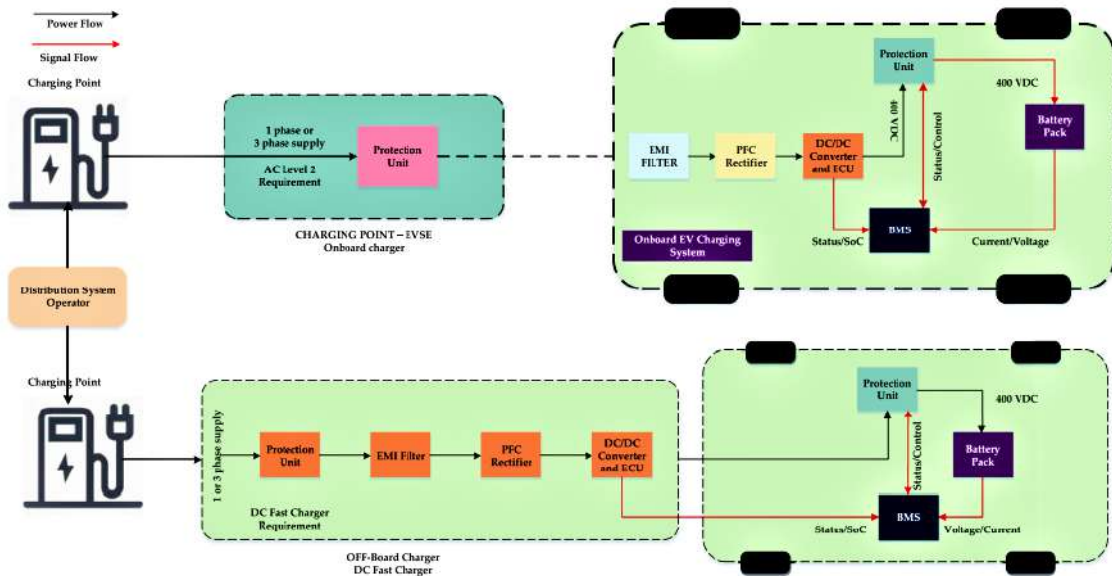
Figure 2.6: A schematic layout of onboard and off-board EV charging systems [14].

2.1.2.2 Wireless Charging

Wireless power transfer (WPT) has been in existence since the late 19th century. Hertz displayed the first demonstration of WPT. Using a spark gap, he demonstrated the propagation of electromagnetic waves in space. Ever since, numerous research teams from across the globe have been investigating the WPT system for use in a variety of applications, including EVs, consumer electronics, mobile phones, laptops, household appliances, medical equipment, and electric machinery A categorization chart for various WPT technologies is shown in Figure 2.7. WPT technology, as can be seen, can be split into four primary categories: near-field transfers, such as inductive, magnetic resonant, and capacitive; far-field transfers, such as laser, microwave, and radio-wave; mechanical force, such as magnetic gear; and acoustic. Capacitive power transfer (CPT) and inductive power transfer (IPT) are the two available wireless charging methods for EVs at the moment.
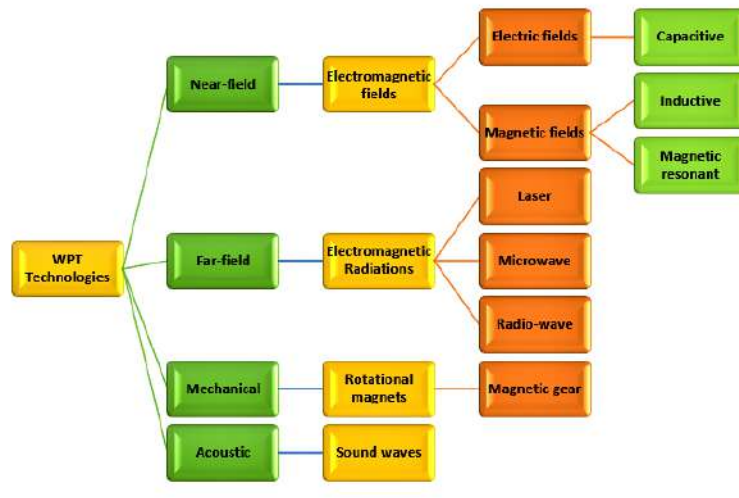
Figure 2.7: A categorization chart for various WPT technologies.

The most often used technique, however, is IPT because it can be employed with a variety of gap lengths as well as power ratings. Contrarily, CPT is only suitable for smaller gap power transfers, although exhibiting promising outcomes with large power levels in kilowatt-level applications. CPT is based on the idea of a capacitor, where a dielectric material-filled air gap is made between the conducting plates. Every half-cycle, an AC excitation reverses the electric field's direction, and the charging and discharging are repeated alternately. The advantages of CPT technology include power transfer over a metal barrier, little eddy current loss, and reduced EMI.

IPT charging technique is the most appealing for EV charging applications because it can transmit high power across a reasonably broad air-gap $(10 - 40cm)$, which satisfies the ground clearance for the most EVs; it is also quiet; has no moving parts, requires no maintenance; is unaffected by impurities; and has electrically isolated parts. Additionally, it can recharge even if the car is moving and does not need a traditional connector (although it requires a standardized coupling technology). Figure 2.8 shows a diagram of the IPT system (IPTS) for EV charging applications [15]. The system contains two electrically separated sides: transmitter and receiver. The grid-rectifier, HF inverter, compensation network, and transmitter coil are stationary components on the primary side that are wired to the power source (grid). The receiver coil, compensation network, and rectifier that are mounted within the car and connected to the battery system make up the secondary side. To receive low-frequency AC power from the grid, the transmitter side is buried in the road. A grid rectifier, a dc link, and an HF inverter are used to convert low-frequency (LF) AC power to high-frequency (HF) AC power. The

transmitter coil then makes use of this converted HF AC to produce an alternating magnetic field. In order to induce HF AC voltages and currents in the secondary circuit, the EMFs produced by the transmitter coil are coupled with the receiver coil (in the vehicle). To charge the vehicle's battery packs, the HF secondary AC power is then rectified. Through a wireless communication link, the two sides (primary and secondary) remain in contact with one another. To minimize the size of the transmitter, receiver, and power converters, the IPT should be utilized at a high frequency. Resonance capacitors create a compensation network that is coupled to both the transmitter and receiver coils for high-efficiency operation. By providing the necessary reactive power for magnetizing this airgap, these capacitors assist in reducing the significant leakage inductances caused by the large airgap.
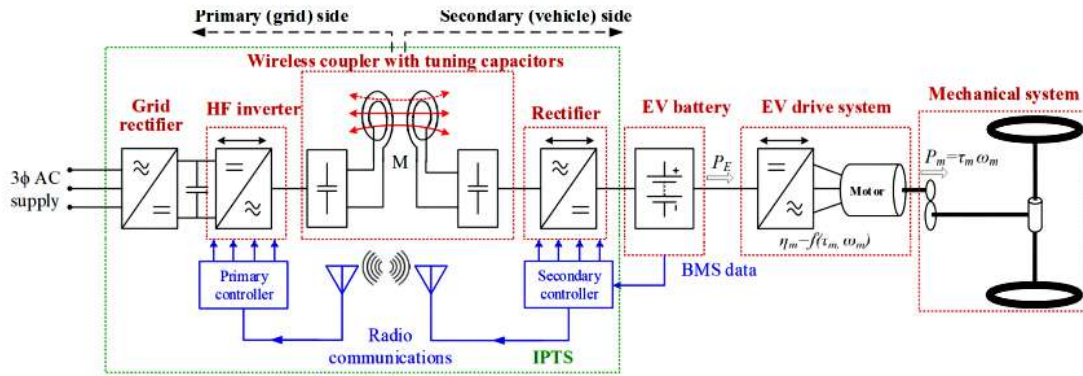
Figure 2.8: A diagram of the IPT system for EV charging applications [15].

Three main forms of IPTS are available for EV charging: static, dynamic, and quasi-dynamic. long term parking places like parking lots, working places, public parking, and home garages are suitable sites to implement static charging. The dynamic charging technology can charge the car steadily as it is moving through specially designated charging lanes along the route, increasing the EV's driving range and minimizing the battery size. The transmitter coil in this situation might either be a long track or a series of linked pads. Due to the high energy requirements of the vehicle and the restricted availability of stops and parking, dynamic charging is the most practical method to support highway travel. Quasi-dynamic charging charges the car when it is briefly halted, as at a traffic signal or a bus stop, expanding the driving range and enabling EVs to store less energy.

The IPT, however, is often not strong. Furthermore, until the transmitter coil is switched off, eddy current loss is another problem with the IPT. Since a real-time connection between the transmitter and the EV is required for data transfer, communication latency is a possibility. Another issue is the cost of implementation.

In comparison to charging by wire, the magnetic couplers and related power electronics will add to the cost. The IPT's electromagnetic field (EMF) can endanger human health and safety by heating human tissue, implanted medical equipment, and metals. Therefore, future research should focus on investigating novel shield designs for safety, lowering implementation costs, designing effective fast chargers, etc.

2.1.2.3 Battery Swap Station (BSS)

One of the fastest and least complicated techniques of charging is the battery swapping or exchange method which is similar to the traditional gas stations. This approach relies on paying the BSS owner a monthly fee for the BMS-enabled battery, which significantly lowers the cost of purchasing electric cars and eliminates the issue of lengthy charging periods. EV owners can use this method to quickly recharge the battery without exiting the vehicle. The BSS's slow charging technique contributes to longer battery life. This BSS system can more easily be integrated with distributed RESs like solar and wind.

Figure 2.9 depicts a BSS's operational structure [16]. EV owners, BSSs, and power grids all communicate with one another through this mechanism. When the EV battery exceeds the charging threshold, a BSS swaps out the depleted battery (DB) for a fully charged battery (FB) before placing the battery in the charging station (BCS). When the charging is finally completed, the BCS sends it back to the BSS for swap in EVs. If the BSS doesn't have any FB, EVs need to wait. One significant feature of BSSs is their ability to do large bidirectional power transfers with the grid. As a V2G system, the FBs can deliver power to the grid during periods of peak demand while charging takes place during off-peak times. However, it also has several drawbacks:
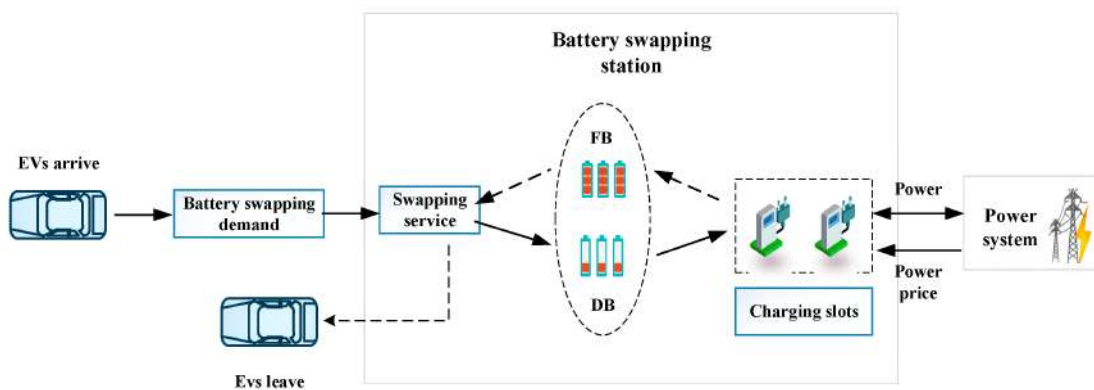
Figure 2.9: An operational structure of a BSS [16].

- High initial outlay: This method necessitates a sizable space to store the batteries, which might require pricey real estate in a busy neighborhood. Batteries are quite expensive; too many batteries raise expenses, while too few batteries can't keep up with demand from customers.

- Hefty cost of EV charging: For EV owners, this method of EV charging might be more expensive than fuelling the ICE engines because of the high monthly rental rates levied by the BSS owner.

- Lack of interoperability: The stations may use a specific battery model, while the EVs may use batteries that differ in standards.

2.1.3 EV Charging Stations

The layout of a charging station with multiple charging nodes is of interest because EV chargers are intended to serve a function similar to that of a traditional fuel station. Keeping this in mind, EV charging stations can be broadly classified as AC or DC charging stations. Figure 2.10 and Figure 2.11 illustrate the two layouts for the EV charging station [14].
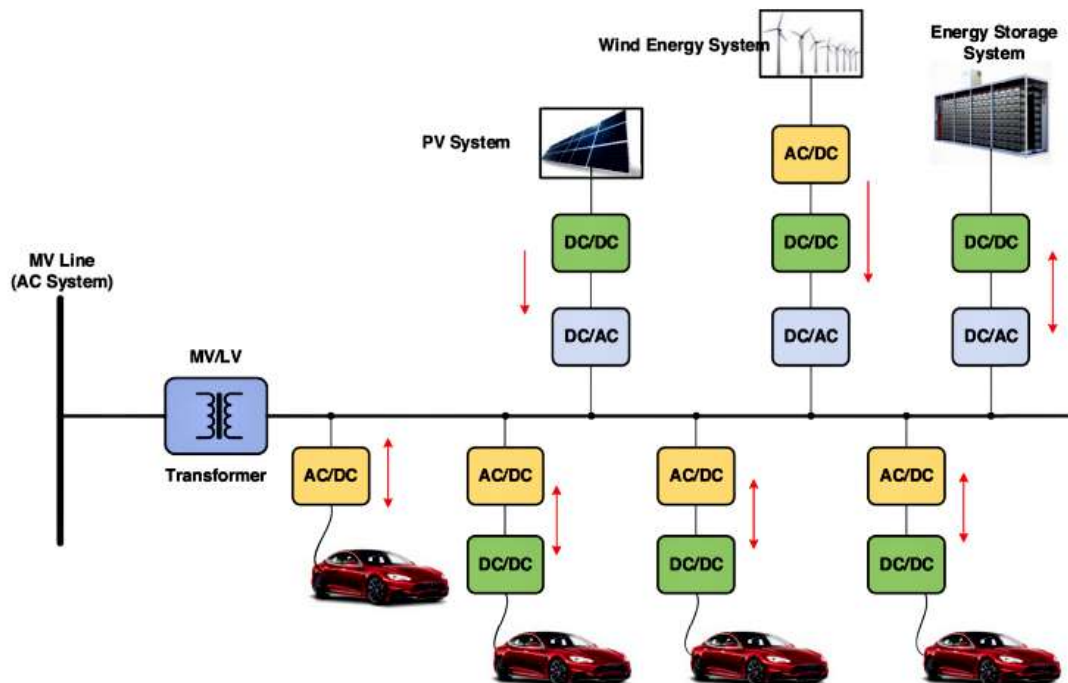
Figure 2.10: A layout for the EV AC charging station [14].
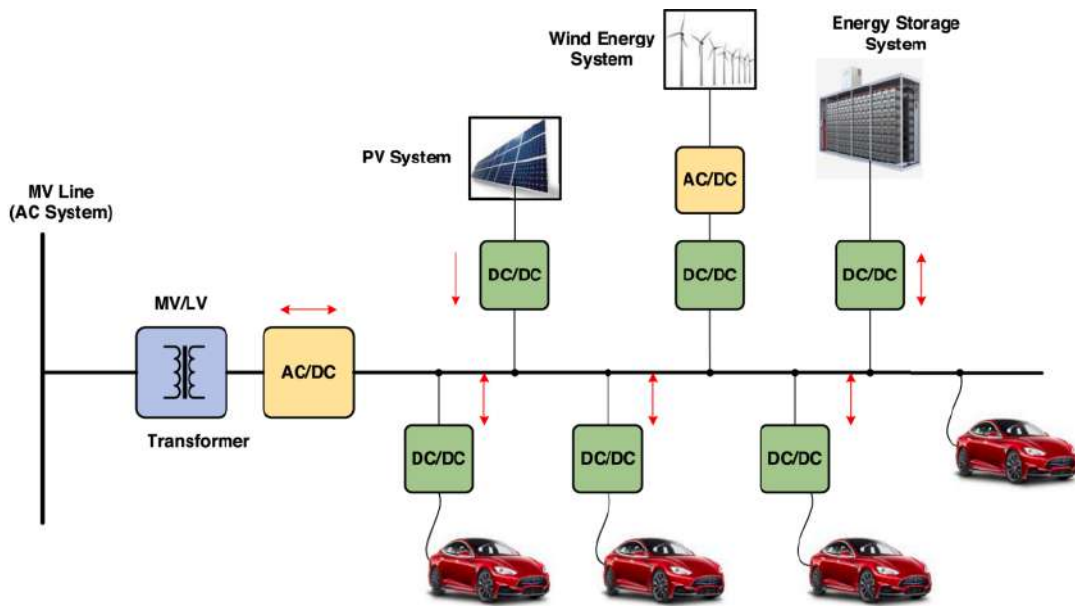
Figure 2.11: An illustration of the EV DC charging station. [14].

2.1.3.1 AC Charging Stations

In the AC charging station, shown in Figure 2.10, a three-phase distribution steps-down transformer transforms the medium voltage (MV) utility supply line into a low voltage (LV) utility supply line (up to 480 V line to line), which serves as a common AC bus for the onboard EV chargers [14]. In contrast to DC fast-charging stations, which use common AC/DC converters attached to the MV-LV step-down transformer, AC charging stations use AC/DC converters that are an integral part of the onboard chargers. These AC/DC converters could be bidirectional, able to feed power to the grid in response to DSO requests. Switchgear cabinets with breakers and disconnectors are used to connect the MV-LV transformer to the AC charging station. This provides the station subsystem with the appropriate protection. Energy storage systems (ESS) and generation capabilities, such as photovoltaic (PV) systems and wind energy systems, can be included in the station system to reduce demand costs paid during peak power consumption at the station. One benefit of an AC charging station is the availability and development of converter technology, switchgear, and protective devices. Another benefit is the existence of well-established standards and procedures for AC distribution systems. The primary drawback of the AC charging station is the need for extra conversion stages (to connect DC loads, DC generator, and ESS to the AC system). These conversion phases make the system more complicated and less efficient. Furthermore, since they must deal with power balance control, voltage control, and frequency control throughout the system's islanded operation,

AC-linked systems are tougher to operate than DC-connected systems.

2.1.3.2   DC Charging Stations

The DC charging station in Figure 2.11 links to the distribution system through a three-phase distribution transformer and an LV bidirectional rectifier stage [14]. The single LV rectifier stage receives electricity from the three-phase distribution transformer at LV AC (up to 480 V line to line) and supplies the dc power to various station subsystems. The rectifier stage offers the DC charging station voltage control, isolation, and bidirectional capabilities. After the rectifier stage, a common DC bus is formed that connects all of the EV chargers in the DC charging station through isolated bidirectional DC/DC converters, providing the necessary isolation and bidirectional facility between the DC bus and the EV ports. The key benefits of dc charging stations are as follows: it removes the need for AC/DC and DC/AC conversion stages, it reduces the number of conversion stages required when transferring power from an ESS to a charger, and it simplifies the integration of RES such as PV and wind energy, as well as ESS that produces dc power. It is also often less expensive and smaller, with higher dynamic performance than AC charging stations. However, because DC voltage does not have natural zero-crossings, developing protective systems for DC fast-charging stations is difficult.

2.2   Power Conversion Topologies for EV Battery Charging Applications

Since converters are a key component of electric vehicles, it is necessary to develop efficient converter designs and to analyze various converter types. With continuous advancements in power electronics technology, particularly in the field of power conversion, the function of converters has enabled researchers to make major contributions to attaining maximum power conversion in EV applications. WBG semiconductors are increasingly used in this EV sector in the modern age. WBG power semiconductors such as SiC and GaN provide several benefits over conventional silicon (Si) devices, including high efficiency, high power density, and superior thermal performance. Figure 2.12 depicts the characteristics of power semiconductor devices made of Si, SiC, and GaN. As a result, WBG semiconductors have recently been used in EV power converters. For instance, as compared to an EV charger with a similar rating based on Si, a 15 kW EV charger based

on SiC supplied 33% more power while taking up 25% less space. Compared to Si device-based isolated converters, it has been proven in [17] that the GaN device-based isolated converter has a volume reduction of 53%, a weight reduction of 79%, an increase in power density of 170%, and an increase in specific power of 500%, as depicted in Table 2.2. As illustrated in Figure 1.11, two types of
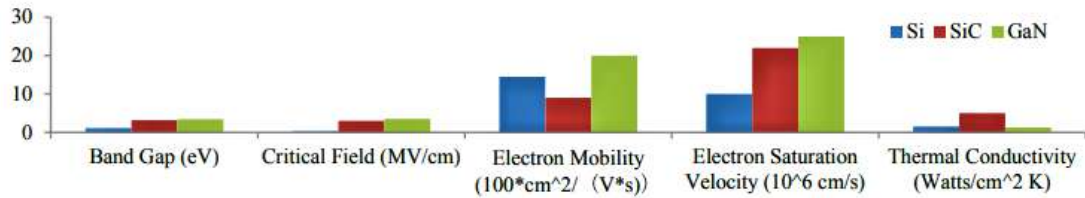
Figure 2.12: The characteristics of power semiconductor devices made of Si, SiC, and GaN [12].

Table 2.2: Comparison of isolation converters based on Si, SiC, and GaN [17]

Specifications	Si isolation converter	SiC isolation converter	GaN isolation converter
Power (kW)	5.2	6.8	6.6
Volume (L)	1.34	1.02	0.63
Mass (kg)	3.27	2.35	0.69
Power density (kW/L)	3.9	6.7	10.5
Specific power (kW/kg)	1.6	2.9	9.6
Peak efficiency (%)	98.4 (40 kHz)	99.0 (100 KHz)	99.0 (100kHz)

power electronics converters are used for EV battery charging: AC-DC converters or rectifiers and DC-DC converters.

2.2.1 AC-DC Converters

Currently, several topologies are used for the front end AC-DC power conversion of EV battery chargers. Figure 2.13 depicts the most recent state-of-the-art AC-DC converters used in EVs. Figure 2.14 displays the circuit diagrams of these various EV-specific AC-DC converters. A comparison of these AC-DC converters is presented in the following Table 2.3. Among the various converters listed, the Vienna rectifier has lower THD and higher efficiency than the others, but it has some drawbacks such as no V2G capability and no galvanic isolation for vehicle safety. Other tabulated converters have some drawbacks that need to be addressed in future research. There is, therefore, plenty of room for future research in the area of AC-DC converters for EVs.

Figure 2.13: AC-DC converters used in EVs.

Table 2.3: Comparison of various AC-DC converters for EV applications.

Converter Topologies	Rated Power (kW)	Maximum Efficiency (%)	Strength	Weakness	Refs.
Bridgeless Isolated Boost	1.7	96.2	• Lesser conduction loss • Higher power capability and high efficiency • Galvanic isolation	• High component count • High input and output ripple • Increased EMI • Unidirectional power flow	[18]
ZVS Interleaved Boost PFC	3	∼98	• Can guarantee ZVS • Higher efficiency • Reduced EMI • Low input and output ripple	• Complex control circuitry • Heating issues for input diode bridge • No Galvanic isolation • Unidirectional power flow	[19]
Bridgeless Interleaved Boost	3.4	98.9	• High efficiency • Reduced output capacitor ripple current • Low power loss	• High component count • High cost • Moderate EMI • No Galvanic isolation • Unidirectional power flow	[20]
Three-phase interleaved SEPIC	4	92	• Modularity	• High conduction loss due to input diode bridge	[21]

Table 2.3: *Continued.*

Converter Topologies	Rated Power (kW)	Maximum Efficiency (%)	Strength	Weakness	Refs.
			• Fault ride through capabilities • Low THD (4.22%) • Provides galvanic isolation • Reduced switching stress	• Hard to keep synchronism between three single phase units • Triplen harmonics due to parametric variation between the three units. • Unidirectional power flow	
Bridgeless SEPIC	0.76	92.1	• Provides galvanic isolation • Low conduction losses • Reduced size and costs	• Unidirectional power flow • High current stress due to DCM mode.	[22]
Totem-pole Interleaved PFC	3.3	98.8	• V2G power transfer facility • Smaller current ripple • Lower EMI • Lower conduction and switching losses	• High cost • No galvanic isolation	[23]
DAB-Based Three-Phase Isolated Converter	1.38	82.1	• Bidirectional power flow • Soft switching of primary and secondary side power converters • Galvanic isolation	• Higher conduction losses • High component count	[24]
Three-Phase Buck-Boost Derived PFC	2	96	• Less control complexity • Less number of sensors • High power density	• High current and voltage stress • No galvanic isolation • Unidirectional power flow	[25]
Bidirectional Series-Resonant Matrix Converter	30	Un-specified	• Bidirectional power flow capability • Galvanic isolation	• High number of switches • Less efficiency	[26]

Table 2.3: *Continued.*

Converter Topologies	Rated Power (kW)	Maximum Efficiency (%)	Strength	Weakness	Refs.
			• High power density due to absence of electrolytic capacitors		
SWISS Rectifier	7.5	96.5	• Low rating devices • Low harmonics • Bidirectional power flow capability	• Number of switches • Less efficiency • Complex controller • No galvanic isolation	[27]
Vienna Rectifier	1.865	99.84	• Low THD (3.25%) • Smaller filtering requirements	• Unidirectional power flow • No galvanic isolation • High output voltage	[28]

2.2.2 DC-DC Converters

The DC-DC converters serve as battery chargers in the back end of EV charging systems. The front-end AC-DC topology accomplishes the rectification operation using PFC, while the back-end DC-DC converter adjusts the voltage level from the rectification operation to make it appropriate for EV battery charging. The design of an EV battery charger presents significant hurdles, including achieving more efficiency, cheaper cost, larger power density, isolation, and satisfying safety criteria. The increased switching frequency allows for a reduction in the cost of passive components. The rationale for limiting the switching frequency is due to high switching losses. As a result, resonant circuits and soft-switching technologies are extensively used to improve the switching frequency. The converter topology used must be capable of controlling the greater output current. Back-end DC-DC converter topologies are classified as isolated or non-isolated based on the presence of galvanic isolation between the input signal and the output circuit. An overview and comparison of the various DC-DC converter topologies used in EV battery charging are provided in this section. Figure 2.15 illustrates the classification of dc-dc converters for EV applications.

(a) Bridgeless Isolated Boost converter [18].

(b) ZVS interleaved boost PFC converter [19].

(c) Bridgeless interleaved boost converter [20].

(d) Three-phase interleaved converter based on SEPIC [21].

(e) Bridgeless SEPIC [22].

(f) Totem-pole Interleaved PFC converter [23].

(g) DAB-based three-phase isolated converter [24].

(h) Three-phase buck-boost derived PFC converter [25].

(i) Bidirectional series-resonant matrix converter [26].

(j) SWISS rectifier [27].

(k) Vienna rectifier [28].

Figure 2.14: Circuit diagrams of various EV-specific AC-DC converters
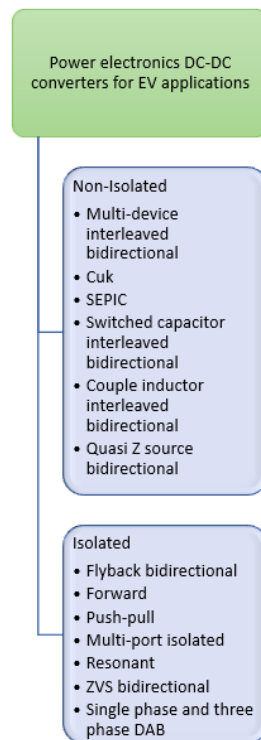
Figure 2.15: DC-DC converters used in EVs.

2.2.2.1 Non-isolated DC-DC Converters

A non-isolated dc-dc converter is one that does not have any electrical isolation between its input and output. These converters are beneficial when dielectric isolation is not a major consideration. These converters have a common ground between their input and output, allowing current to flow between them. Non-isolated converters are often used when the voltage has to be stepped up or down by a relatively modest ratio. These converters are better suited for use in mid- and high-range vehicles. Non-isolated converters have higher efficiency, lower cost, and less control complexity than isolated converters. They, too, have certain downsides. They cannot provide protection against high electrical voltages and produce greater noise. As a result, there are safety concerns with non-isolated converters. These converters can be characterized as unidirectional or bidirectional based on their capacity to reverse power flow. There are five basic types of non-isolated DC-DC converters that are frequently used: multi-device interleaved bidirectional, Cuk, SEPIC, switched capacitor interleaved bidirectional, coupled inductor interleaved bidirectional, and quasi Z-source bidirectional. The circuit schematics of these non-isolated converters are shown in Figure 2.16. Table 2.4 contains a comprehensive analysis and comparison of these converters. As can be seen, each of the tabulated converters has its own set of strengths and drawbacks. One of

these converters' common strengths is the ability to provide bidirectional power flow, which is critical for V2G applications. Table 2.4 summarizes the converters' other strengths and weaknesses. Hopefully, future research will focus on these shortcomings to enhance their performances.

2.2.2.2   Isolated DC-DC Converters

To electrically separate the input and output side voltages for safety or regulatory reasons, isolated DC-DC converters employ galvanic isolation. For instance, if the input side is linked to voltages that are high enough to put people in danger, safety regulations may mandate the use of an isolated DC-DC converter, which transfers voltage and current using a transformer (or, in some circumstances, coupled inductors) across the gap between the input and output terminal. Again, these isolated DC-DC converters are beneficial for removing ground loops, which will help to isolate noise-sensitive circuitry from the noise sources. Conversely, utilizing a transformer for isolation might result in design tradeoffs, most notably costs, size, performance instability, and assembly issues. Isolated DC-DC converters are widely used in low- and medium-power automotive applications. Flyback bidirectional, forward, push-pull, multiport isolated, resonant, ZVS bidirectional, single-phase and three-phase DAB are some of the key isolated DC-DC converters used in EV applications. Figure 2.17 depicts the circuit diagrams for these isolated converters. Table 2.4 provides a comprehensive evaluation and comparison of these isolated converters. Except for the forward converter, all of these converters are capable of bidirectional power flow, which is required for V2G operation. Resonant and DAB converters are among the tabulated converters that are growing in popularity because of their high efficiency and ZVS operation. Each set of converters has its own set of strengths and weaknesses. Hopefully, future research will address these weaknesses to improve the converters' efficiency for EV battery charging applications.
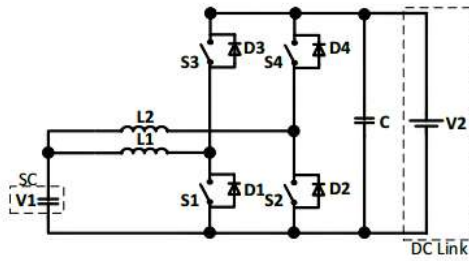
(a) Multidevice Interleaved Bidirectional Converter [29].
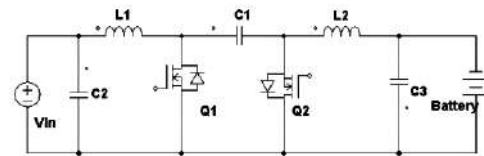
(b) Cuk Converter [30].
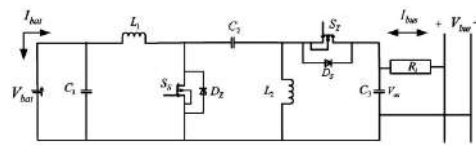
(c) SEPIC [31].
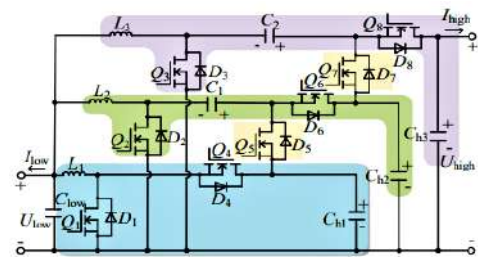
(d) Switched Capacitor Interleaved Bidirectional Converter [32].
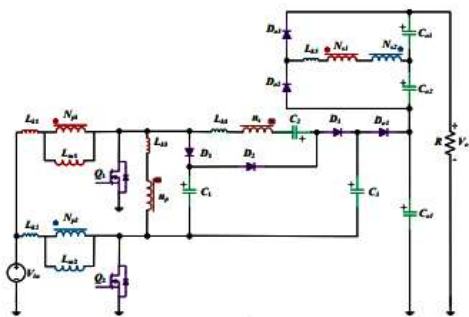
(e) Coupled Inductor Interleaved Bidirectional Converter [33].
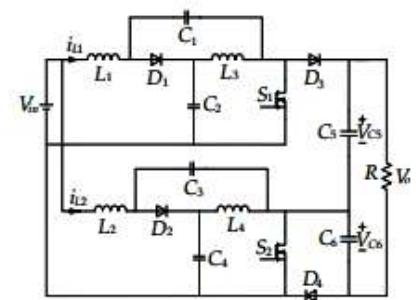
(f) Quasi Z-Source Bidirectional Converter [34].

Figure 2.16: Circuit schematics of various EV-specific Non-isolated DC-DC converters
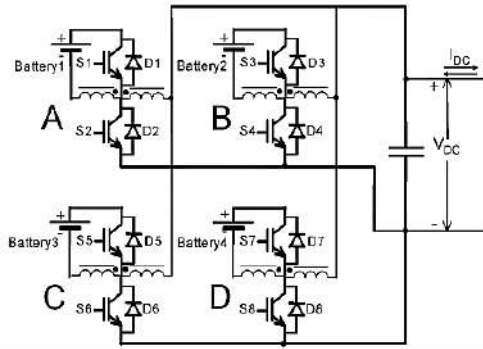
(a) Flyback Bidirectional Converter [35].
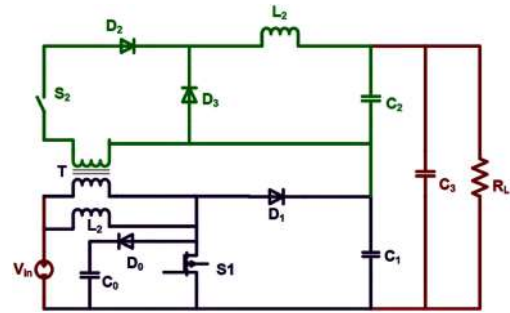
(b) Forward Converter [36].
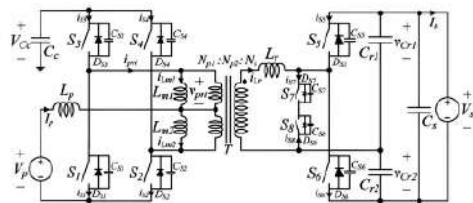
(c) Push Pull Converter [37].
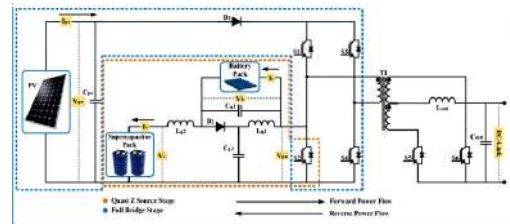
(d) Multiport Isolated Converter [38].
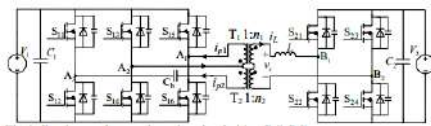
(e) ZVS Bidirectional Converter [39].
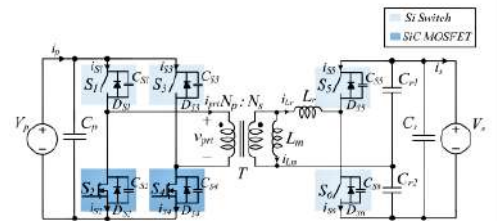
(f) Resonant Converter [40].
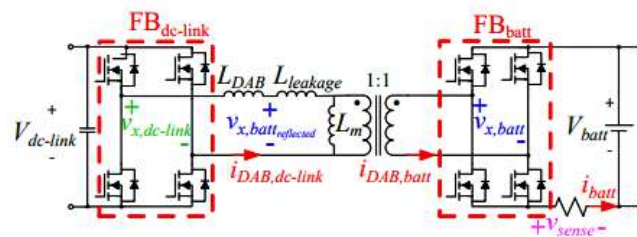
(g) Single Phase and Three Phase DAB Converter [41].

Figure 2.17: Circuit diagrams of various EV-specific Isolated DC-DC converters

Table 2.4: Comparison of various DC-DC converters for EV applications.

Converter Types	Converter Topologies	Rated Power (kW)	Maximum Efficiency (%)	Strength	Weakness	Refs.
Non-isolated	Multidevice Interleaved Bidirectional	150	98	• High efficiency • Reduced component size • Lower current stress • Bidirectional power flow	• Complex analysis during transient and steady-state conditions • No galvanic isolation	[29]
	Cuk	0.85	94	• Continuous and reduced ripple current at input and output • Improved PF • Bidirectional power flow possible with modified cuk	• Larger inductors subjected to higher electrical stress • High-voltage rating for the transfer capacitor • High number of passive components • No galvanic isolation	[30]
	SEPIC	1.5	98	• Gate drive circuitry is less complicated. • Less voltage stress than CUK • Non-pulsating input current • Bidirectional power flow possible with modified SEPIC	• No Galvanic isolation • High current stress in diode and switches	[31]
	Switched Capacitor Interleaved Bidirectional	0.8	95.9	• Topology scalability • Wide voltage gain range • Low current ripple on the low voltage side	• High current ripple • No galvanic isolation	[32]

Table 2.4: *Continued.*

Converter Types	Converter Topologies	Rated Power (kW)	Maximum Efficiency (%)	Strength	Weakness	Refs.
				• Low voltage stress across power switches • Common ground between input and output • Bidirectional power flow capability		
	Coupled Inductor Interleaved Bidirectional	4.5	98.67	• Wide voltage conversion ratio • Reduced current and voltage ripple • Lower current rating of power components • lesser components • Increased efficiency • Bidirectional power flow capability	• Leakage inductance causing voltage and current spikes • No galvanic isolation between input and output	[33]
	Quasi Z-Source Bidirectional	0.4	96.44	• Bidirectional power operation • Reduced voltage stress • Wide voltage gain range • Common ground between input and output • Continuous input current	• No galvanic isolation • High cost due to higher number of components	[34]
Isolated	Flyback Bidirectional	6	∼96	• Bidirectional power flow	• High ripple current	[35]

Table 2.4: *Continued.*

Converter Types	Converter Topologies	Rated Maximum Power (kW)	Efficiency (%)	Strength	Weakness	Refs.
				• Suitable for high voltage step-up situations • Fewer number of components • Capable of working with multiple power sources • Topology scalability • Galvanic isolation	• High voltage stress due to leakage inductance • Unsatisfactory utilization of the transformer	
	Forward	5	95.4	• High efficiency • Fast balancing time • Easy to control • Less number of components and circuitry • Galvanic isolation	• Nonuniform secondary voltage • Limited maximum duty cycle during the transformer reset process due to peak flux reaching higher levels during startup and transient states • Unidirectional power flow	[36]
	Push Pull	22	96.85	• Low conduction losses • Less filtering is required • Galvanic isolation • Bidirectional power flow capability	• Additional circuitry required for soft switching • Protection required during switching • Imbalance magnetic flux	[37]

Table 2.4: *Continued.*

Converter Types	Converter Topologies	Rated Power (kW)	Maximum Efficiency (%)	Strength	Weakness	Refs.
	Multiport Isolated	9.6	96	• Bidirectional power flow capability • Galvanic isolation • Low output voltage ripple current • Wide voltage gain • Reduced number of circuit components	• High sensitivity in response to duty cycle under load changes • It is challenging to achieve accurate synchronization.	[38]
	ZVS Bidirectional	3.5	96.8	• Achieves ZVS under all load conditions • Low EMI • High power density • Easy control • Galvanic isolation • Bidirectional power flow	• Inadequate fault tolerance	[39]
	Resonant	3.5	97.8	• High efficiency • High conversion ratio • Bidirectional power flow • Galvanic isolation • ZVS	• Complex integrated transformer	[40]
	Single Phase and Three Phase DAB	6.6	∼99	• Bidirectional power flow • Galvanic isolation • High power density	• Circulating current in the high-frequency transformer and power switches • Higher pulsating current at the input side • Limited range of soft switching	[41]

Table 2.4: *Continued.*

Converter Types	Converter Topologies	Rated Maximum Power (kW)	Efficiency (%)	Strength	Weakness	Refs.
				• ZVS • Low voltage and current stresses		

Chapter 3

Proposed Converter Design and Modeling

This chapter explains the design process for the proposed asymmetric CLLL resonant DC-DC converter with a high voltage gain for EV battery charging and discharging applications. A closed-loop controller has also been developed to control and stabilize the output voltage. Over a wide battery voltage range, the developed converter can accomplish soft switching in both forward and reverse working modes, offering great efficiency in G2V and V2G applications.

3.1   Operating Principles

The structure of an isolated bidirectional asymmetric resonant CLLL converter is depicted in Figure 3.1. Both charging (G2V, or Grid to Vehicle), and discharging (V2G, or Vehicle to Grid,) modes are possible with the converter. Two full-bridge converters with four switches each make up this CLLL converter. To accomplish inversion, the S14, as well as S23 switches, are activated in the forward direction at 50% duty cycle. S58 and S67 will achieve rectification with their antiparallel diodes. GaN transistors have inherent reverse conduction capabilities, hence antiparallel diodes are not necessary when using them as switching devices. Only the reverse conduction of Si, SiC MOSFET, and IGBT transistors necessitates antiparallel diodes. In one operation period, the CLLL resonant converter has four stages. The driving circuit's operational scenarios are identical in both forward and backward directions; only the resonant components differ. In the following subsections, the operating principles of the proposed CLLL converter are investi-
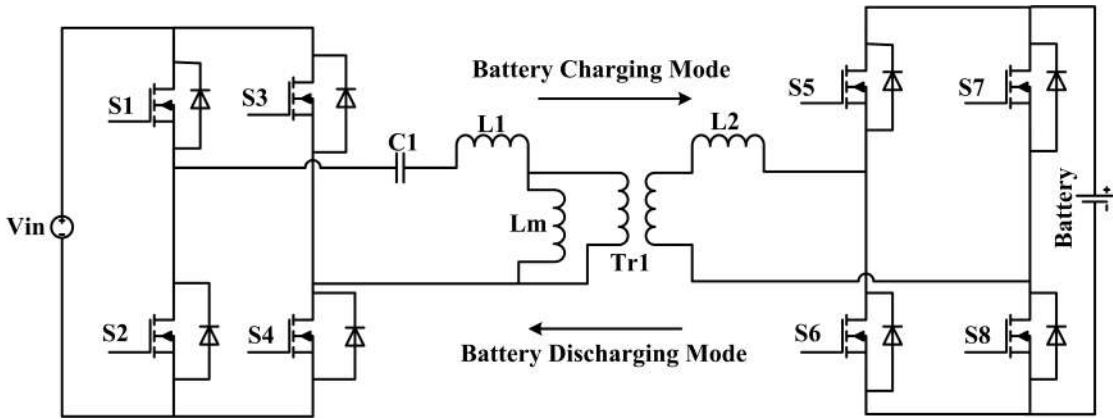
Figure 3.1: Structure of isolated bidirectional CLLL Resonant DC-DC Converter.

gated in both forward and reverse power flow modes.

3.1.1   Forward Operating Modes

The battery is charged in forward power flow mode. Figure 3.2 illustrates the forward operational modes of the proposed bidirectional CLLL resonant converter. As illustrated in Figure 3.2, the converter has four operational modes during a single switching cycle. Modes 1 and 2 are repeated with different switch and rectifier pairs to Modes 3 and 4. Modes 1 and 3 are for dead-time durations, while Modes 2 and 4 are for resonance and power transfer. The primary switches operate in the inverting mode while power is transferred from the primary to the secondary side; however, the secondary switches turn OFF and operate as rectifiers in the rectifying mode. Figure 3.3 shows the theoretical waveforms of the proposed converter for all modes during a single switching cycle. In Figure 3.3, there are only the waveforms of the forward operating mode. All of the forward operating modes are thoroughly explained in this subsection.

Mode 1 $[t_1 - t_2]$: This is a dead-time duration mode. The primary resonant current i_p passes through the anti-parallel diodes of S1, S4 switches and feeds back to the input source, causing the switches to operate in the ZVS mode.

Mode 2 $[t_2 - t_3]$: S1, S4 switches are turned on in this mode. The voltage across the transformer T_{r1} secondary causes the body diodes of the secondary switches S5, S8 to become forward-biased, and power is transferred to the battery via the rectifier bridge. Because the input voltage source V_{in} forces the primary current to a positive direction through the S1, S4 switches, the primary current changes its direction to positive. During mode 2, T_{r1} sees the output voltage on the secondary side, and the magnetic energy of the magnetizing inductance, L_m, is

(a) Mode 1

(b) Mode 2

(c) Mode 3

(d) Mode 4

Figure 3.2: Forward operational modes of the proposed bidirectional CLLL resonant converter. The black lines represent the current conduction path, whereas no power flows along the grey path.

Figure 3.3: Waveforms of proposed CLLL converter in the forward direction.

built up linearly. As a result, initially, L_m does not participate in the resonance. Mode 2 will end when i_p meets i_{Lm}, indicating the completion of the resonance operation that transfers power from the primary to secondary sides. As a result, the secondary current, i_s is zero. ZCS is achieved when the secondary side current, i_s reaches zero while the diodes of the switches S5, S8 are turned off. At this time, L_m, along with the series inductor L_1 and capacitor C_1, participates in the resonance. The magnetizing energy will accumulate until the switches S1, S4 are turned off.

Mode 3 $[t_3 - t_4]$: This mode, like mode 1, has a dead-time duration with the switch pair S2, S3. The operation in this mode is similar to mode 1; under the ZVS condition, the primary current passing through the antiparallel diode of the switch pair S2, S3 can cause those switches to turn on.

Mode 4 $[t_4 - t_5]$: The S2, S3 switches are activated, and the converter begins to transfer power from the primary to the secondary sides. During this mode, i_p changes direction for the same reason as in mode 2. Mode 4 performs the same operation as mode 2 but with a different switch pair of S2, and S3. The resonance and power transfer are turned off at the end of mode 4. Without power transfer through T_{r1}, i_s becomes zero, and the antiparallel diode pair of S6, S7 is softly commuted, resulting in ZCS in the same way as mode 2.

3.1.2   Reverse Operating Modes

During reverse power flow mode, the battery discharges. The full bridge converter on the battery side functions as an inverter in this mode, converting the battery voltage to a high-frequency square wave. On the DC bus side, full wave rectification of the square wave is accomplished by using the antiparallel body diode pair of switches S1 to S4, which are turned off during reverse operation. During a single switching cycle, the converter has four operational modes, as shown in Figure 3.4.

As can be seen, modes 3 to 4 in the second half cycle are symmetrical to modes in the first half cycle. Power is transferred from the EV battery to the DC bus in modes 1 through 4 except when i_p meets i_{Lm}; modes 1 and 3 are dead time intervals. The antiparallel diode pair of S5, S8, and S6, S7 switches are softly commuted in modes 1 and 3, allowing ZVS operation. To facilitate ZCS operation, the antiparallel diode pairs S1, S4, and S2, S3 are softly commuted in modes 2 and 4.

(a) Mode 1

(b) Mode 2

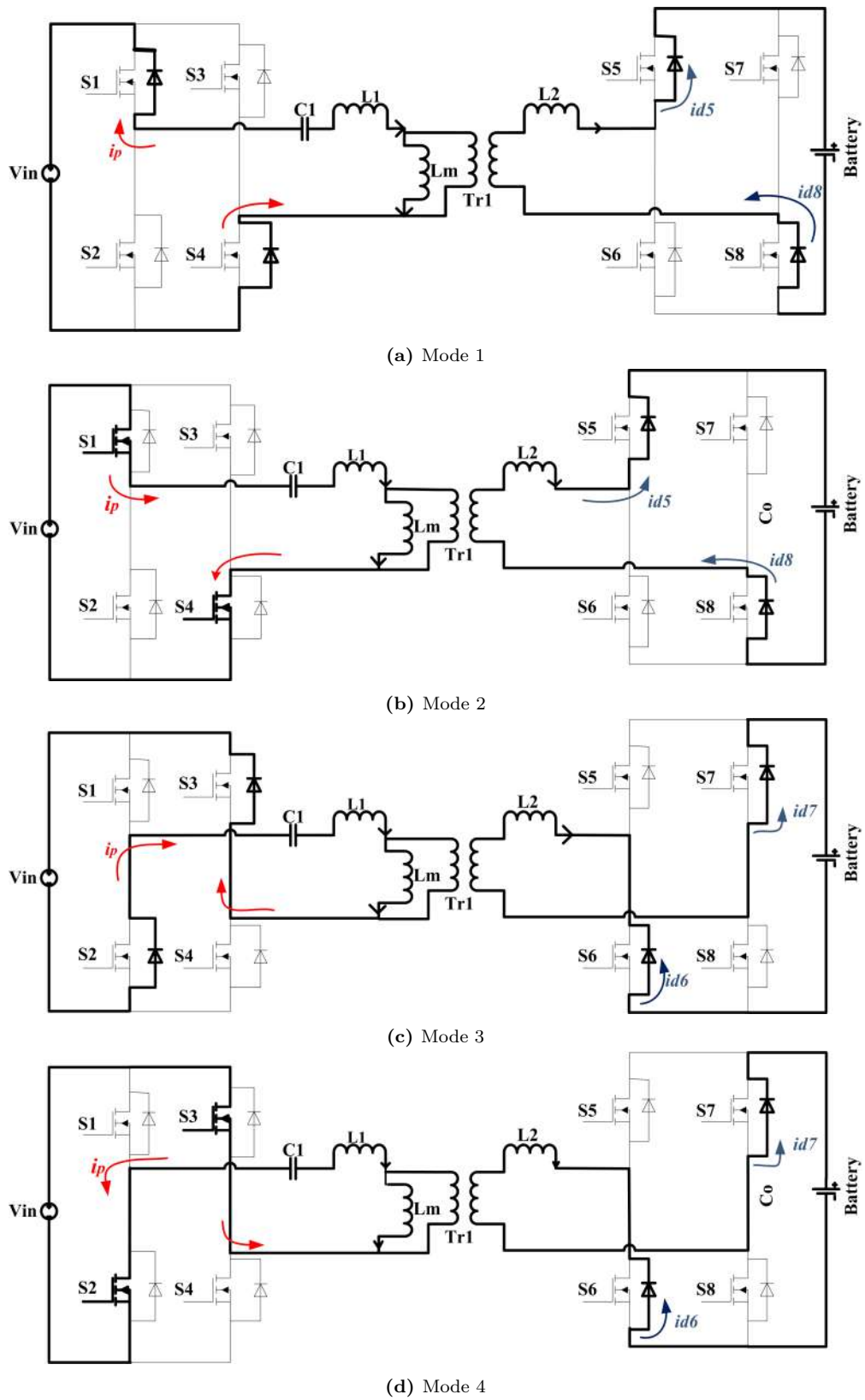**(c)** Mode 3

(d) Mode 4
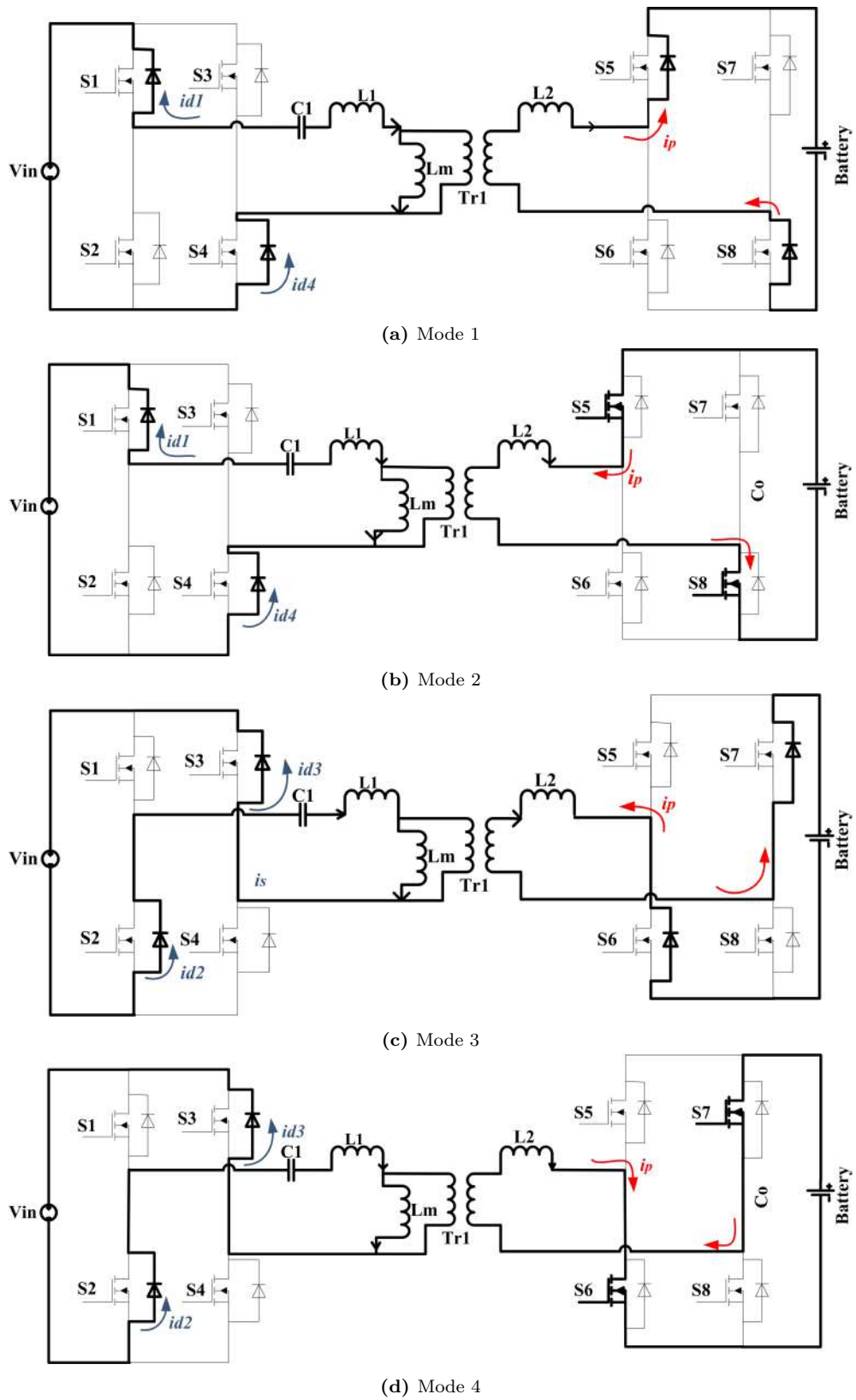
Figure 3.4: Reverse operational modes of the proposed bidirectional CLLL resonant converter. The black lines represent the current conduction path, whereas no power flows along the grey path.
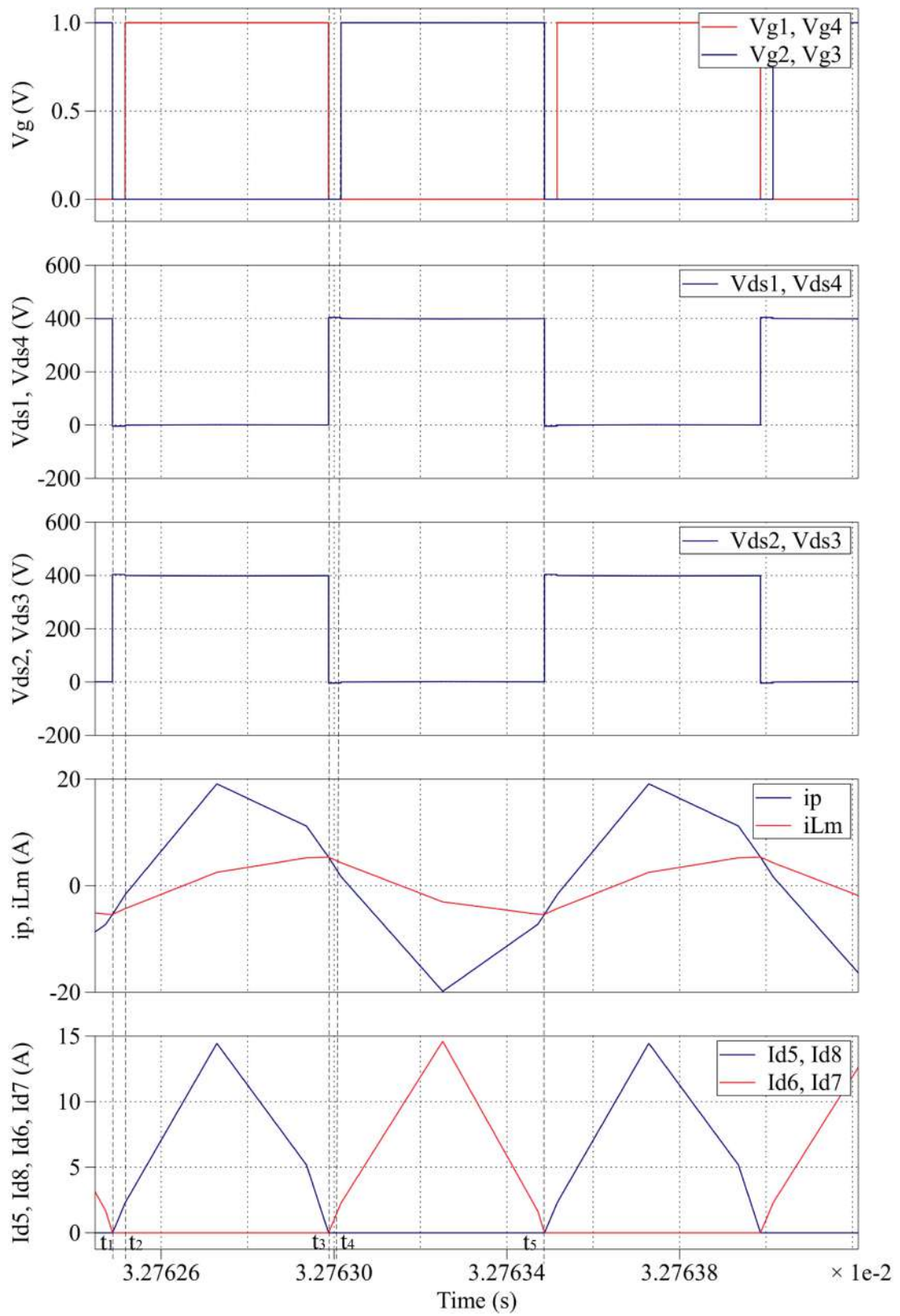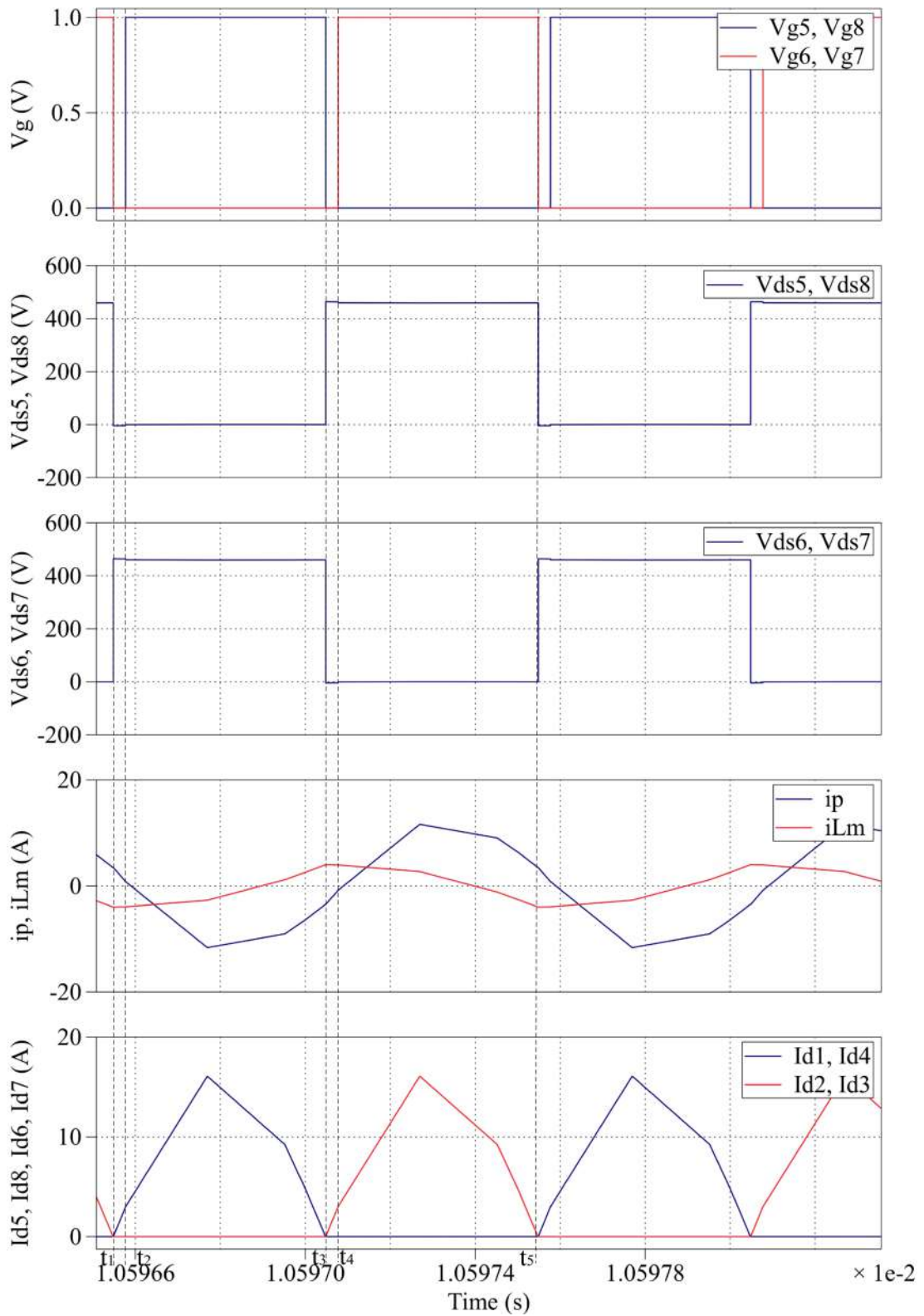
Figure 3.5: Waveforms of proposed CLLL converter in the reverse direction.

The waveforms of the converter in the reverse direction are plotted in Figure 3.5. As can be seen from Figure 3.3 and Figure 3.5 the operating principles and the waveforms of the converter in both operating modes are essentially the same.

Following a thorough examination of the operational procedures, it is revealed that the CLLL resonant dc-dc converter can achieve ZVS on primary-side semiconductor switches as well as ZCS on secondary-side semiconductor switches.

3.2   Proposed Converter Design

The converter design includes finding the turns ratio of the transformer (n), formulating the magnetizing inductance (L_m), capacitances (C_1), resonant inductances (L_1 and L_2), and developing a PSPWM-based optimized controller.

3.2.1   Design of the Transformer's Turns Ratio

Resonant dc-dc converters are most efficient at the self-resonant frequency, f_r. As a result, the converter ought to operate at this frequency under typical operating circumstances. The transformer's turns ratio can then be determined by calculating as,

$$n = \frac{N_1}{N_2} = \frac{V_{in_{nom}}}{V_{o_{nom}}} \tag{3.1}$$

where the transformer's primary and secondary turns ratio, nominal input, and output voltage are represented by $N_1, N_2, V_{in_{nom}}, V_{o_{nom}}$ respectively.

3.2.2   Design of the Resonant Components

Figure 3.6 displays the proposed CLLL converter's equivalent circuit model in both directions. The components of the resonant tanks are L_1, L_2, L_m, and C_1. When the converter is operating at its self-resonant frequency, the total impedance is pure resistance. As a result, at self-resonant frequency, the converter's reactive impedance should be zero. The following equation can be derived from Figure 3.6:

$$-j\frac{1}{\omega_r C_1} + j\omega_r L_1 + \frac{j\omega_r(L_m n^2 L_2)}{L_m + n^2 L_2} = 0 \tag{3.2}$$

(a) Charging mode.

(b) Discharging mode.
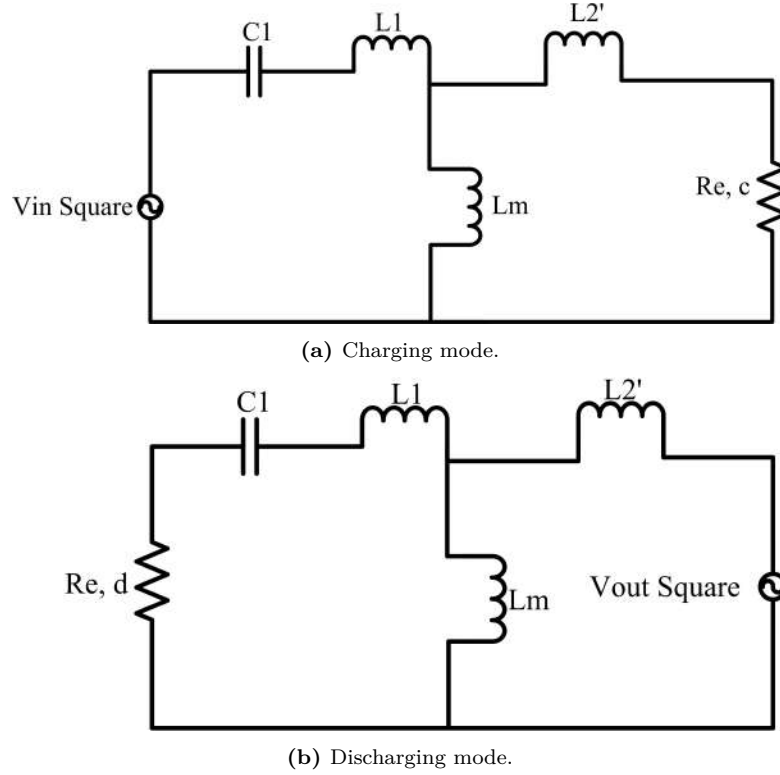
Figure 3.6: Equivalent circuit model of the proposed CLLL resonant converter.

By simplifying Equation 3.2, the self-resonant frequency can be obtained, as shown in Equation 3.3.

$$f_r = \frac{1}{2\pi\sqrt{C_1(L_1 + \frac{L_m n^2 L_2}{L_m + n^2 L_2})}} \tag{3.3}$$

Let Re, L_2' be the corresponding equivalent R_o, L_2 of the CLLL converters, and here, R_o stands for the converter's output load resistance. It is possible to calculate the equivalent load resistance by using the First Harmonic Approximation (FHA) technique. For the G2V or battery charging mode, L_2' and Re, c of the converter can be calculated as follows:

$$L_2' = n^2 L_2, \qquad Re, c = \frac{8n^2}{\pi^2}R_o \tag{3.4}$$

The parameters for the V2G or battery discharging mode will be the same, and they are as follows:

$$L_2' = \frac{L_2}{n^2}, \qquad Re, d = \frac{8}{n^2\pi^2}R_o \tag{3.5}$$

By keeping the current flowing through primary-side switches negative at the time of turn-on, ZVS in these switches can be ensured. The primary current ought to be able to completely charge and discharge the output capacitors of the primary switches during the dead time. The magnetizing inductance L_m and the length of

the dead time determine the amount of this current. Therefore, the primary side switches' ZVS is controlled by the magnetizing inductance L_m, output capacitance of switches (C_{oss}), operating frequency, and dead time (t_{dead}). This converter performs in dead time like an LLC resonant dc-dc converter. This allows the magnetizing inductance to be expressed in a manner that is similar to that of the full-bridge LLC resonant dc-dc converter. Here is this expression [42]:

$$L_m \leq \frac{t_{dead}}{16 C_{oss} f_{s,max}} \tag{3.6}$$

where the highest switching frequency is indicated by $f_{s,max}$.

Under various load conditions, a relatively low magnetizing inductance L_m, guarantees ZVS in primary-side switching devices. On the other hand, L_m can never be set too low. Too little L_m would cause the magnetizing current to be extremely high, which would result in significant conduction losses, higher primary side capacitor peak voltage requirements, and higher apparent power requirements for switching devices. A low magnetizing current is produced by a high magnetizing inductance, but the converter's voltage gain is constrained. Consequently, the magnetizing inductance L_m should not be too high.

The dead time between switching devices has an impact on the ZVS range as well. ZVS will be easier to achieve for a broad range of input and output voltages with higher dead time. Additionally, by uplifting the inductance with a long dead time, the magnetizing current could be decreased. On the other hand, a relatively high dead time will cause a high primary RMS current because there will be no transfer of energy during the dead-time duration. All of these issues must be kept in mind when designing the magnetizing inductance L_m.

Figure 3.7 depicts the fluctuation of the converter voltage gain over a range of normalized frequencies (f_r/f_s ratio) with varied loading circumstances, i.e., different quality factors, $Q = \frac{\sqrt{\frac{L_1}{C_1}}}{R_e}$. As a result, the output voltage can be regulated by modifying the converter's switching frequency f_s. Within a suitable switching frequency range, the converter can function in the inductive area (as illustrated in Figure 3.7), where the switch voltage leads the tank current waveform, ensuring that the voltage returns to zero before the current rises and so ensuring ZVS.
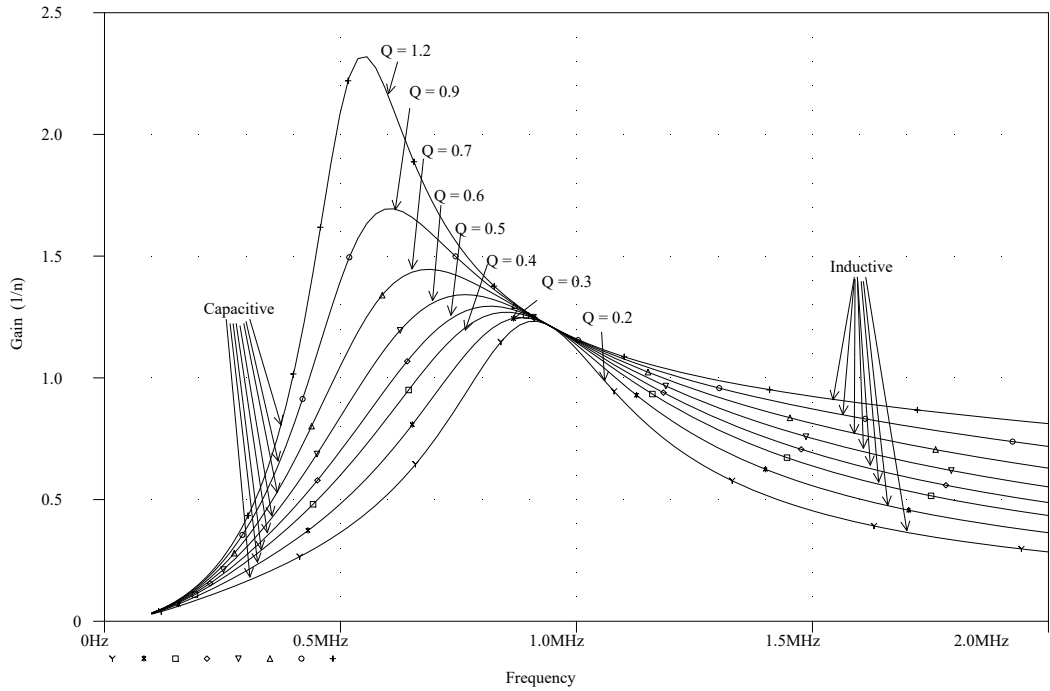
Figure 3.7: Gain waveforms of CLLL converter for different loading conditions.

3.2.3 Estimated Design Parameters

In G2V mode, the input voltage range is $400 - 460V$, while the output voltage range is $530 - 610V$. Correspondingly, in the V2G mode, the input voltage range is $530 - 610V$, while the output voltage range is $400 - 460V$. The nominal operating frequency in the charging and discharging modes is $1MHz$. The resonant frequency is set at $1MHz$. To step up the input voltage, the transformer turns ratio, n is set to $\frac{400}{530} \cong 0.8$ according to Equation 3.1. Load resistance can be calculated from $\frac{V_{o2}}{P}$ equation, where V_o and P are the expected output voltage and power, respectively. From Equation 3.3, 3.4, 3.5, and 3.6 the resonant parameters $L_1, L_2, L_m,$ and C_1 can be determined, producing:

$$L_1 = 3.49\mu H, \qquad L_2 = 4.62\mu H, \qquad L_m = 21.5\mu H, \qquad C_1 = 3.91nF \qquad (3.7)$$

3.2.4 Design of the PSPWM-based Controller

For the regulation and stabilization of output voltages, an efficient closed-loop controller has been designed. An optimized PID controller has been developed

first, followed by an intelligent controller based on deep reinforcement learning. The detailed design process of the two controllers will be provided in the following sections.

3.2.5   PID Controller

The proposed discrete-time PID controller's block schematic, which is based on PSPWM, is provided below in Figure 3.8. The three main components of the con-
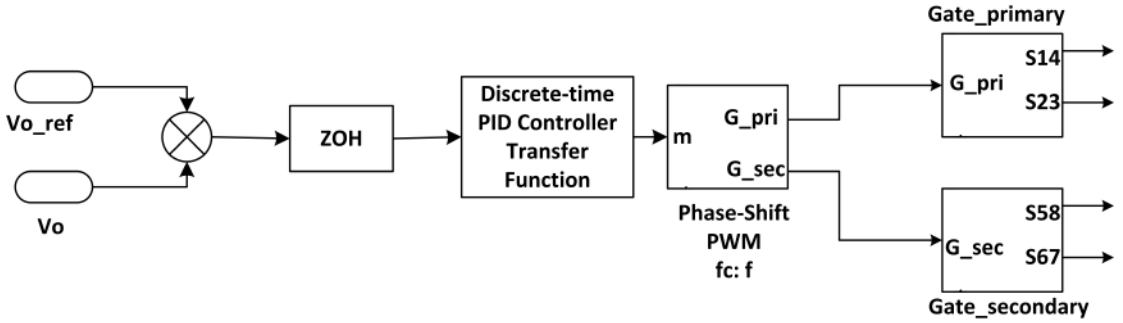
Figure 3.8: Block schematic for a PID controller.

troller are the 'ZOH' (Zero Order Hold) block, the 'Discrete-time PID Controller Transfer Function' block, and the 'Phase Shift PWM' block. The difference signal between the reference and actual output voltage levels is sampled by the 'ZOH' block and stored there. The output voltage is then stabilized and regulated by the 'Discrete-time PID Controller Transfer Function' block using proportional, integral, and derivative control. The following Equation 3.8 can be used to represent the transfer function of a discrete-time PID controller in the Z domain:

$$C(z) = K_p + \frac{K_i T_s z}{z - 1} + \frac{K_d N(z - 1)}{(1 + N T_s)z - 1} \tag{3.8}$$

Where $K_p, K_i,$ and K_d stand for the proportional, integral, and derivative gains of the proposed PID controller, respectively, T_s is the sampling period, and N is the parameter of the first-order filter on the derivative term. Once more, Equation 3.8 can be changed to yield the following:

$$C(z) = \frac{b_0 + b_1 z^{-1} + b_2 z^{-2}}{a_0 + a_1 z^{-1} + a_2 z^{-2}} \tag{3.9}$$

which has the following coefficients:

$$b_0 = K_p(1 + NT_s) + K_i T_s(1 + NT_s) + K_d N \tag{3.10}$$

$$b_1 = -(K_p(2 + NT_s) + K_i T_s + 2K_d N), \qquad b_2 = K_p + K_d N \tag{3.11}$$

$$a_0 = (1 + NT_s), \qquad a_1 = -(2 + NT_s), \qquad a_2 = 1 \tag{3.12}$$

Two optimization techniques, Genetic Algorithm (GA) [43] and Particle Swarm Optimization (PSO) [44], were used to optimize the PID controller parameters. Their step responses were also compared for the stability analysis. Because PLECS excels at power electronics system level simulation and MATLAB is required for controller optimization, MATLAB and PLECS co-simulation were used in this work. In the GA, the search for the optimal solution space mimics the way natural selection drives biological evolution. It repeatedly adjusts a population of individual solutions and, at each step, picks people from the current population to be parents and utilizes them to generate offspring for the following generation. The population progresses toward an optimal solution over subsequent generations by achieving the best fitness value. ITAE (Integral of Time Weighted Absolute Error) is employed as the fitness function in this case. Algorithm A.1 provides the pseudocode for the GA algorithm. Figure 3.9 shows the minimum observed fitness value as the genetic algorithm solver progresses. The optimized controller parameter by the genetic algorithm is given in the following.

$$K_p = 11.0956, \qquad K_i = -12.7484, \qquad K_d = -3.8236, \qquad N = 3.0057 \tag{3.13}$$

PSO, like GA, is a population-based algorithm. The main advantage of the PSO is that it can find the best solution with the least amount of computation. This PSO algorithm is inspired by swarming flocks of birds or insects. Based on an objective function, each particle is drawn to some extent to the best place it has located thus far, as well as the best location found by any member of the swarm. After a few iterations, the population may congregate around a single site, a few spots, or continue to migrate. Algorithm A.2 provides the pseudocode for the PSO algorithm. Figure 3.10 shows the minimum observed fitness value as the PSO algorithm solver progresses. The optimized controller parameter by the PSO algorithm is given in the following.

$$K_p = -0.7053 \times 10^4, \quad K_i = -0.0555 \times 10^4, \quad K_d = 0.2595 \times 10^4, \quad N = -0.0664 \times 10^4 \tag{3.14}$$

The step response performance of these two optimization algorithms is compared
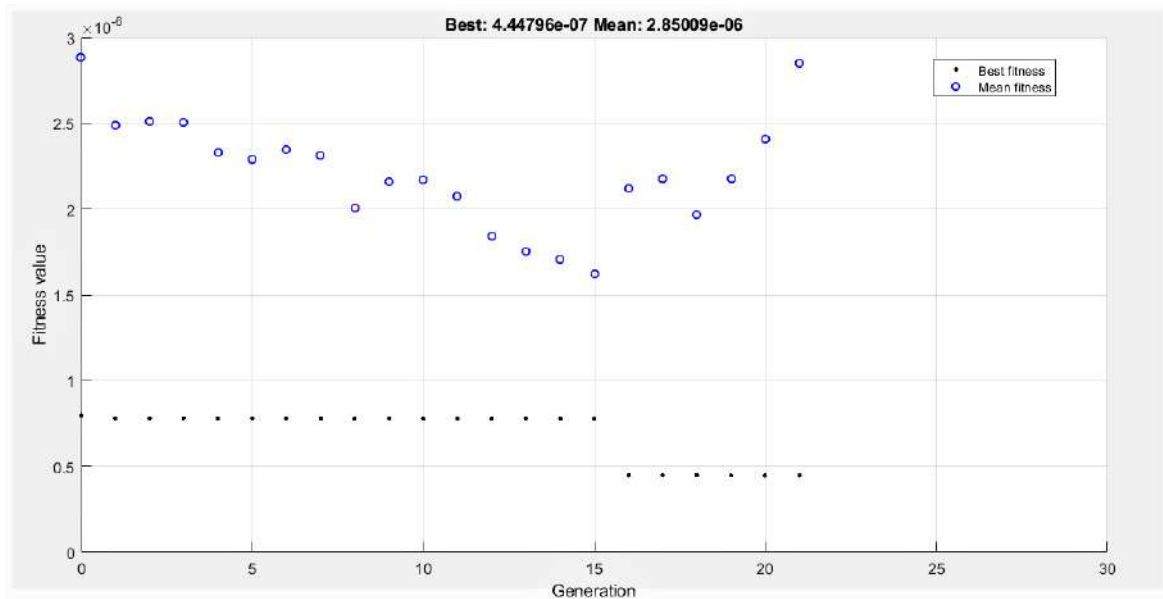
Figure 3.9: Fitness value in genetic algorithm optimization.
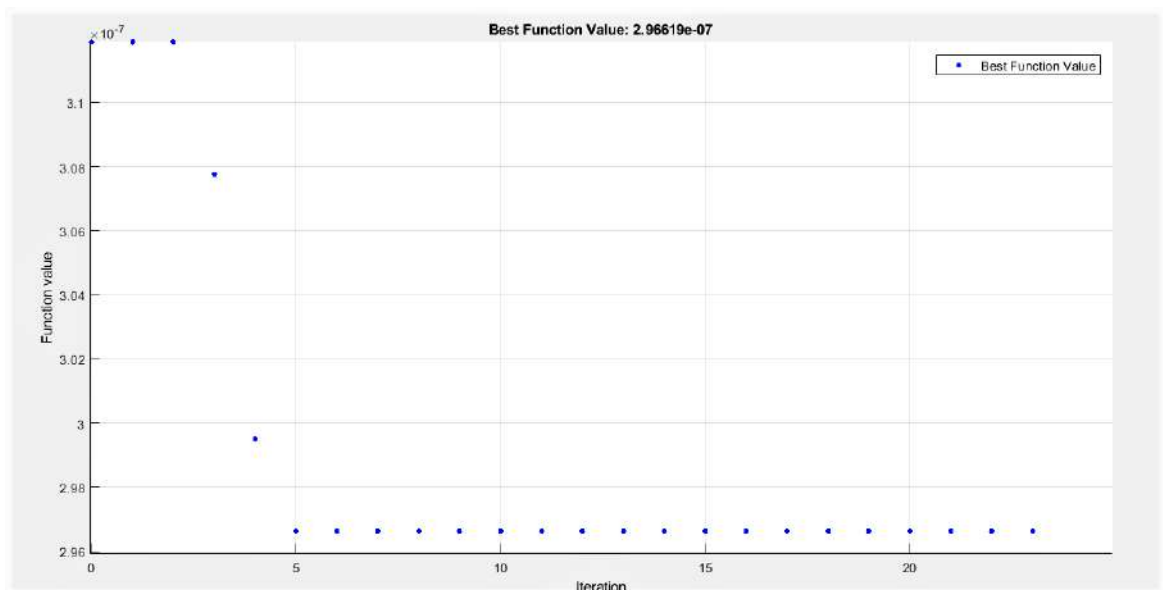
Figure 3.10: Fitness value in PSO algorithm optimization.

in Table 3.1. According to Table 3.1, both optimization techniques performed similarly and satisfactorily. In some aspects, the GA PID controller performed better than the PSO PID controller, which converged faster with less computation. As a result, when it comes to fast computation, the PSO PID controller outperforms the GA PID controller. As shown in Figure 3.8, The Phase Shift PWM block uses

Table 3.1: Step response performance of GA and PSO-optimized PID controller

Step Response Characteristics	Plant with GA PID Controller	Plant with PSO PID Controller
Rise Time (s)	1.5265e-05	1.5260e-05
Transient Time (s)	8.2185e-05	8.2388e-05
Settling Time (s)	8.2185e-05	8.2388e-05
Settling Min (V)	480.4168	480.4168
Settling Max (V)	648.2221	648.2221
Overshoot (%)	22.0123	22.0997
Undershoot (%)	0	0
Peak (V)	648.2221	648.2221
Peak Time (s)	3.0107e-05	3.0107e-05
ITAE	4.448e-07	2.9662e-07

the PSPWM technique in the output signal of the PID controller. It sends the pulse signal that switching devices require in order to stabilize and regulate the output voltage signal. Figure 3.11 depicts the block diagram of the PWM subsystem. The PID output signal is compared with two sawtooth PWM carrier signals with a 180-degree phase shift between them to generate the phase-shifted PWM control signal waveform for the switches. The final gate signals for the switches are generated by the SR flip-flop block. The internal block diagram of the SR flip flop is shown in Figure 3.12. It was built with a pair of cross-coupled NOR logic gates.

3.2.6 Deep Reinforcement Learning for Intelligent Control of Proposed Converter

In EV powertrains, DC-DC bidirectional resonant power converters are extremely nonlinear and prone to uncertainty, disturbance, and instability generated by local surroundings. Because conventional PID controllers are only effective for a restricted operational range of nonlinear systems, they are ineffective for managing this sort of DC-DC bidirectional resonant power converters. Again, the conventional PID has weak tolerance to model parameter uncertainty. As a result, the conventional PID controller will be inadequate for controlling the proposed DC-DC CLLL converter. Furthermore, global optimization techniques such as PSO and GA are computationally costly and are applied offline for benchmark-
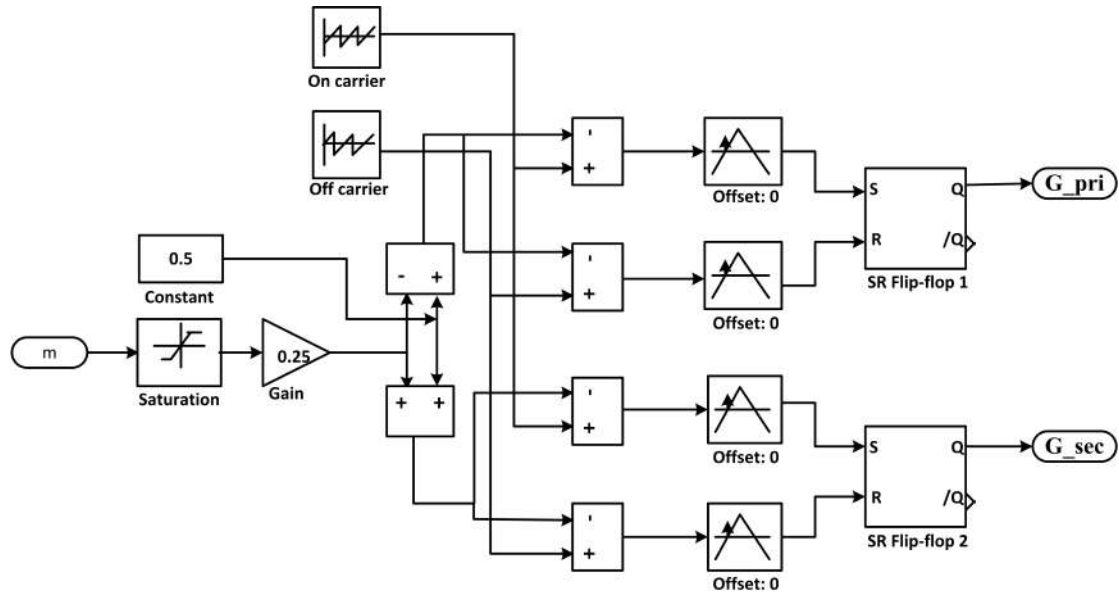
Figure 3.11: Phase shift PWM block diagram.
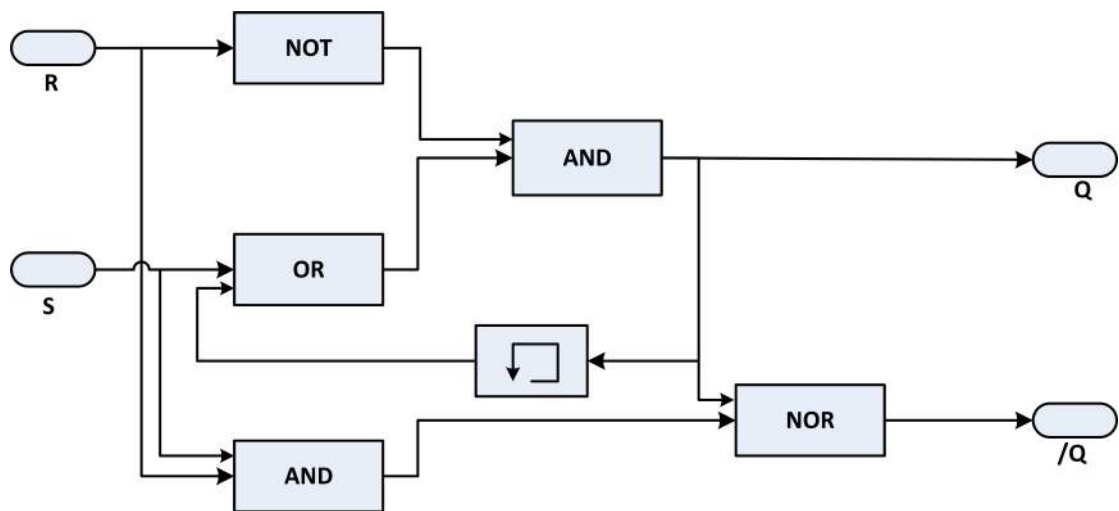
Figure 3.12: SR flip-flop block diagram.

ing purposes. Real-time optimum control can alleviate the problems associated with global optimization approaches by transforming the process into an instantaneous one. Several model-based strategies have been developed to provide real-time optimum control, including model predictive control (MPC), sliding mode controller (SMC), linear matrix inequality (LMI) controller, and Fuzzy logic controller. However, un-modeled dynamics, which cannot be represented using deterministic mathematical methodologies, make dc/dc converter control design challenging and prevent model-based strategies from projecting exactly or performing adequately. The rationale for developing a model-independent controller for resonant BDCs is that such systems are plagued by model errors, quantization effects, and uncertainties in practice. To overcome this limitation, model-independent data-driven approaches such as deep neural networks (DNNs) and deep reinforcement learning (DRL) have been formulated to cope with uncertain or partially unknown dynamics. Due to their restricted learning power, DNNs become inadequate at approximating the uncertain model of resonant BDCs. DRL can be a useful solution for overcoming the constraints of previously used approaches. In contrast to conventional control systems, DRL has the advantage of improved self-learning through an interactive approach based on observational data from a dynamic environment. DRL can make judgments and solve realistic control challenges. For instance, Deep Q Network (DQN) can train an action-value function using DNNs and DRL in an iterative manner by applying a Bellman equation. The DQN is emerging as a strong data-driven scheme to perform challenging problems, such as controlling autonomous underwater vehicles, and autonomous aerial vehicles (AAV). This is due to the considerable advancement of several novel methodologies including experience replay and mini-batch learning in training the DNNs. However, it is not feasible to directly employ DQN in continuous action spaces since obtaining the best policy in continuous spaces needs optimization at each time step. As a result, given large, unrestrained function approximators and fairly complex action spaces, this optimization is just too slow to be feasible [45]. In order to overcome the drawbacks of the DQN algorithm's operation in continuous action spaces, Lillicrap et al. [45] created the 'Deep Deterministic Policy Gradient' (DDPG) algorithm. Although DDPG occasionally achieves excellent performance, it is typically fragile in terms of hyper-parameters and other types of tuning. A prominent failure scenario for DDPG is that the learned Q-function tends to substantially overestimate value functions, resulting in a suboptimal policy that leverages the Q-function errors [46]. The 'Twin Delayed DDPG' (TD3) method tackles this problem by making three modifications [46]:

- Clipped Double Q learning: TD3 learns two Q-value functions rather than one (thus the term "twin") and employs the lesser of the two Q-values when updating policy.

- Delayed Policy Updates: TD3 delays policy and target network updates in order to minimize value error. This leads to higher-quality policy revisions.

- Target Policy Smoothing Regularization: TD3 introduces a tiny amount of random noise to the target policy to make it more difficult for the policy to exploit Q-function errors by smoothing out Q along with fluctuations in action.

Recently, DRL has received a lot of attention from the research community. This DRL algorithm is being used in a variety of applications. However, only a few research studies have shown how effective DRL algorithms are as an intelligent control strategy for DC-DC converters. For instance, Cui et al. [47] utilized the 'Markov Decision Process' (MDP) model and the DQN algorithm to solve the problem of DC-DC buck converter stability issues. It has been proved that the proposed control technique greatly reduces the settling time in the event of a disturbance. In [48], DDPG was utilized for online adjustment of the 'Active Disturbance Rejection Controller' (ADRC), which regulates an IoT-based DC-DC buck converter serving constant power loads (CPLs). Tang et al. [49] developed a DDPG-aided minimal reactive power control system based on the harmonic analysis approach to minimize the reactive power for the DAB converter.

In this context, this research proposes a DRL controller as the optimal control method for the proposed resonant BDC for applications involving the charging of EV batteries. By engaging directly with the converter and learning optimal control without having to precisely model the resonant BDC, this controller provides better control than the conventional PID controller. But, it is not always practical to attach the actual, physical EV charger to a computer and allow the DRL agent to communicate with the converter in order to learn. To train the DRL agent, it is common to use approximate modeling and simulation of the controller plant as nearly as feasible. In this work, the DRL agent is trained using this methodology. Initially, the environment model for the DRL agent has been put up using a 'MATLAB Simulink' model paired with 'PLECS Blockset'. 'The PLECS Blockset' was used to model the converter circuit so that practical conduction loss, switching loss, and thermal impedance data of switches from the manufacturer's PLECS model could be easily added. Second, the DRL agent was trained using MATLAB's newly released 'Reinforcement Learning Toolbox'. To

train the DRL agent, the TD3 algorithm was used. The DRL agent creates the PSPWM signals required by the switches to maintain the proposed converter circuit's voltage stability. Lastly, a DRL-PID validation circuit has been designed and simulated in order to compare the performance of the DRL controller with that of the conventional PID controller.

3.2.6.1 Deep Reinforcement Learning: A Brief Overview

This section provides a brief overview of DRL followed by an overview of the TD3 algorithm.

Key Concepts and Terminology in DRL Framework DRL involves learning how to act in order to accomplish a goal through interaction. The *agent* and the *environment* are the key elements of the DRL. The *agent* is the DRL algorithm's learner and decision-maker. The *environment* is everything that surrounds the agent and with which it interacts. A sequential decision-making process is used by the DRL *agent* and its *environment*. They interact in a discrete time-step sequence. For a specific task, the *agent's* actions represent the decisions it makes, the *states* serve as the foundation for those decisions, and the *rewards* serve as the standard by which those decisions are evaluated. The *environment* creates *rewards*, which are used by the *agent* to judge how good or bad the current state is. The goal of the *agent* is to maximize the cumulative *reward*, also known as *return*, by reinforcing good actions over the poor in order to learn an optimal *policy*. The *agent* knows and is entirely in control of everything that is within it; nevertheless, it might or might not be fully aware of all that is outside. The key elements of DRL are depicted in Figure 3.13 below. As shown in Figure 3.13, the
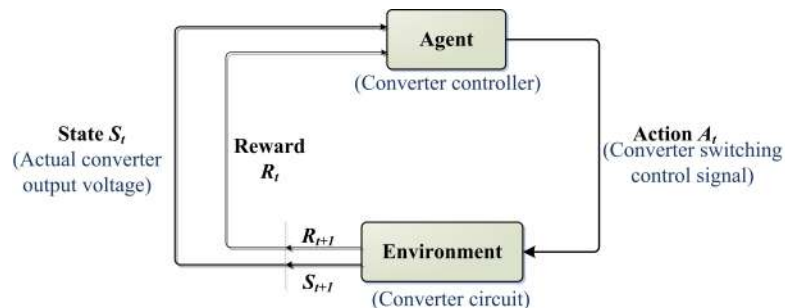
Figure 3.13: Basic DRL block diagram.

agent gets the state of the environment, S_t, at every time step t and chooses an action, A_t, based on that state. The agent gets a quantifiable reward, R_{t+1}, for its actions at time step $t + 1$, and as a result, is in a different state, S_{t+1}. The

Markov decision process (MDP) is a term used to describe this kind of framework of sequential decision-making processes. The probability of changing into state s' at time t can be expressed by the following state transition probability function for certain values of the prior state and action, as well as for specific values of these random variables, s' and r:

$$p(s', r|s, a) \doteq Pr\{S_t = s', R_t = r|S_{t-1} = s, A_{t-1} = a\} \tag{3.15}$$

DRL's terminologies agent, environment, and action are analogous to the control system nomenclature controller, controlled system (or plant), and control signal respectively. For the proposed converter, the controller or agent delivers the control signals (switching signals) required to regulate and stabilize the converter's or plant's output voltage signal.

Returns   The return is the total of the rewards over the last time step T. It can be formulated using the subsequent Equation 3.16.

$$G_t \doteq R_{t+1} + R_{t+2} + R_{t+3} + ... + R_T \tag{3.16}$$

Discounted Returns   Discounting affects the current worth of future rewards. In this technique, the agent prioritizes present rewards above future rewards when determining the return objective. Following Equation 3.17 gives an expression for the discounted return.

$$G_t \doteq R_{t+1} + \gamma R_{t+2} + \gamma^2 R_{t+3} + ... = \sum_{k=0}^{\infty} \gamma^k R_{t+k+1} \tag{3.17}$$

where γ represents the discounted return and $0 \leq \gamma \leq 1$.

Policies and Value Functions   A policy is a guideline that governs how an agent chooses actions based on states. The policy functions as the DRL agent's brain. It could be either deterministic or stochastic. The deterministic policy is represented by μ, while the stochastic policy is represented by π. Equations 3.18 and 3.19 express the deterministic and stochastic policies, respectively. This research examines the deterministic policy.

$$a_t = \mu(s_t), \tag{3.18}$$

$$a_t \sim \pi(\cdot|s_t). \tag{3.19}$$

Knowing a state's or state-action pair's 'value' is crucial in DRL. And value functions are state (or state-action pair) functions that estimate how good it would be for the agent to be in a certain state. In this case, 'how good' is defined in terms of expected return. The following value function Equation 3.20, v_π, links the value of s to the value of its probable successor states for any policy, π and any state, s:

$$
\begin{aligned}
v_\pi &\doteq \mathbb{E}_\pi[G_t|S_t = s] \\
&= \mathbb{E}_\pi[R_{t+1} + \gamma G_{t+1}|S_t = s] \\
&= \sum_a \pi(a|s) \sum_{s'} \sum_r p(s', r|s, a)[r + \gamma \mathbb{E}_\pi[G_{t+1}|S_{t+1} = s']] \\
&= \sum_a \pi(a|s) \sum_{s',r} p(s', r|s, a)[r + \gamma v_{\pi(s')}]
\end{aligned}
\tag{3.20}
$$

The Bellman equation for v_π is given in Equation 3.20. The value function v_π is the only solution to its Bellman equation. The DRL algorithms' approximate computation and learning of v_π are dependent on this Bellman equation for v_π.

Optimal Policies and Optimal Value Functions   Finding a policy that produces significant long-term rewards is roughly what it means to solve a DRL problem. There is at least one policy that is always superior to other policies and whose value functions are optimum. This is referred to as an *optimal policy*. Many optimum policies may exist. and they can be represented by π_*. The *optimum value functions* assign the highest expected return possible by any policy to any state or state-action pair. The optimal policies all have the same optimal state value and optimal action-value function. The state value function, v_* is defined by Equation 3.21 below.

$$
v_*(s) \doteq \max_\pi v_\pi(s)
\tag{3.21}
$$

Similarly, the following Equation 3.22 can be employed to define the action value function, q_*.

$$
q_*(s) \doteq \max_\pi q_\pi(s)
\tag{3.22}
$$

3.2.6.2   The TD3 Algorithm-Based DRL Controller

Fujimoto et al. [46] discovered that function approximation errors in DRL methods such as Double DQN and DDPG result in overestimated value estimates and suboptimal policy. To address the drawbacks of DQN and DDPG, they developed the TD3 algorithm. The TD3 algorithm is a DRL approach that is model-free, online,

and off-policy. The algorithm will be examined in three steps in the paragraphs that follow.

1. **Clipped Double Q-learning:** First of all, the TD3 algorithm mimics the original Double Q-learning formulation's concept. It employs two actors $(\pi_{\phi_1}, \pi_{\phi_2})$ and two critics $(Q_{\theta_1}, Q_{\theta_2})$, with π_{ϕ_1} being optimized in relation to Q_{θ_1} and π_{ϕ_2} being optimized in relation to Q_{θ_1} [46]. This is expressed by Equations 3.23 and 3.24 [46].

$$y_1 = r + \gamma Q_{\theta'_2}(s', \pi_{\phi_1}(s')) \tag{3.23}$$

$$y_2 = r + \gamma Q_{\theta'_1}(s', \pi_{\phi_2}(s')) \tag{3.24}$$

Both Q-functions employ a single target update, computed using the smaller of the two Q-functions [46]:

$$y = r + \gamma \min_{i=1,2} Q_{\theta_{i'}}(s', \pi_{\phi'}(s')) \tag{3.25}$$

The value target in this Clipped Double Q-learning cannot contribute any additional overestimation when compared to the regular Q-learning target [46]. Then, by regressing towards that value target, both Q functions are learned using the loss function Equation 3.26.

$$L(\theta_i) = \frac{1}{N} \sum_{j=1}^{N} (y_j - Q_{\theta_i}(s_j, a_j))^2 \tag{3.26}$$

2. **Delayed Target Policy Updates:** Second, target networks were employed in the algorithm to give a steady goal in the learning process while also allowing for more convergence in the training data. Without such target networks, every update generates some residual TD (temporal difference) error, resulting in error buildup and divergence in training data. Yet, the usage of rapidly updating target networks leads to extremely divergent behavior when the policy is trained on the current value estimate [46]. Because of this, the policy updates in this TD3 algorithm have been sufficiently delayed to update the policy with a low variance value estimate.

3. **Target Policy Smoothing:** A learning target using a deterministic policy is highly susceptible to inaccuracies caused by function approximation error when updating the critic, increasing the target's variance [46]. This is addressed by a regularizer known as target policy smoothing, which mimics the SARSA learning update. The target policy was given a small amount

of random noise and averaged over mini-batches. This led to the following modified target update [46]:

$$y = r + \gamma \min_{i=1,2} Q_{\theta_{i'}}(s', \pi_{\phi'}(s') + \epsilon),$$
$$\epsilon \sim \text{clip}(\mathcal{N}(0, \sigma), -c, c). \tag{3.27}$$

where the added noise was clipped to maintain the target near to the original action. Algorithm A.3 presents a pesudocode of the TD3 algorithm [46].

3.2.6.3 DRL Controller Experimental Setup

This section explains the DRL controller's design process. First, an environment model was developed for the DRL controller's training. As the DRL agent, a TD3 agent has been employed. Following the training of the TD3 agent, an experimental setup was established to compare the controller's performance to that of traditional GA and PSO-optimized PID controllers. This DRL controller was designed using MATLAB Simulink's 'Reinforcement Learning Toolbox' and PLECS Blockset software.

Environment Model for Training TD3 Agent   The proposed CLLL resonant DC-DC Converter model serves as the environment model in this work. This control system's objective is to maintain the converter's output voltage at a level that is consistent with a reference value in the presence of disturbances. The PLECS Blockset software was utilized to create the environment model. As a switching device for the converter, a PLECS model of E-mode GaN HEMT from GaN Systems Inc. was used. Figure 3.14 depicts a PLECS Blockset circuit block that serves as the environment model for training the TD3 agent. The block is made up of the proposed CLLL converter circuit model.

Observation and Action Spaces   The TD3 agent is trained in the environment with the observation and action spaces. The observation vector $[\int e\,dt\ e]^T$ forms the observation space for the TD3 agent. Here, $e = Vo_{ref} - Vout$ represents the tracking error signal of the DRL agent, while Vo_{ref} and $Vout$ represent the reference output voltage and actual output voltage of the proposed CLLL converter, respectively. The two most important observation input signals used in training DRL controllers are instantaneous error and integral error. The instantaneous error has no memory, whereas the integral error has the memory of previous
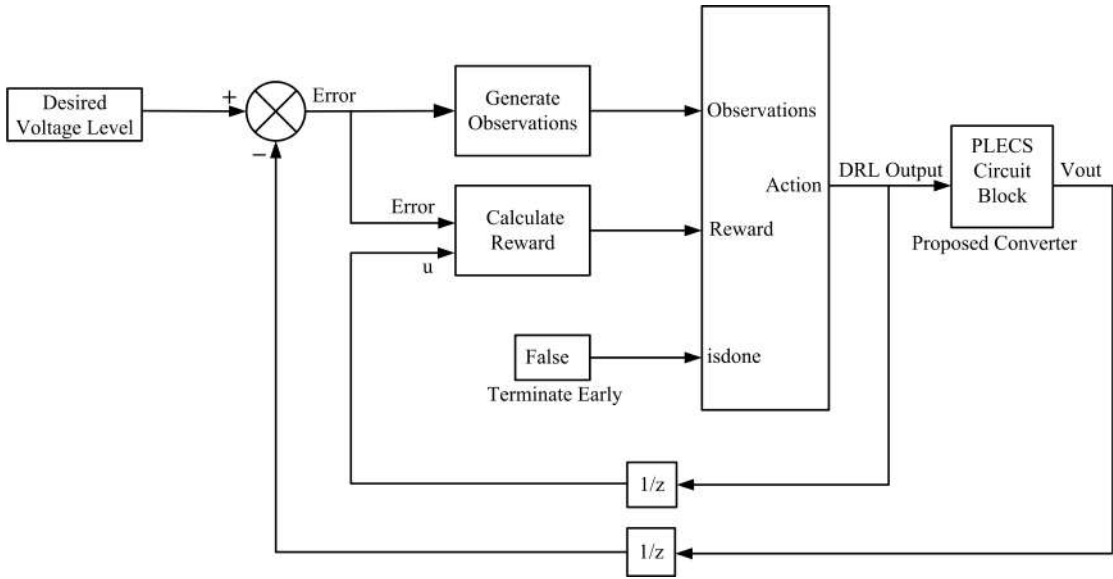
Figure 3.14: DRL controller training setup.

errors. Integral error drives the DRL agent to reduce error to zero and aids in more effective agent training. As we can see, the observation signal is shown in Figure 3.14 connected to the TD3-based DRL agent block. This TD3-based DRL agent has a continuous action space that provides the required switching signals via a phase shift PWM block. As can be seen in Figure 3.14, the action signal is linked to the PLECS Blockset circuit block.

Reward Function for TD3 Agent A reward function can be discrete, continuous, or hybrid. The agent in this work has been trained to reduce the error to zero using a hybrid reward function. The reward function has been defined as a function of instantaneous error. The discrete reward function is shown in Equation 3.28 that follows.

$$
\begin{aligned}
\text{Reward}, r = 10, \qquad & \text{if } |e(t)| < \lambda \\
= \frac{1}{|e(t)|}, \quad & \text{else.}
\end{aligned}
\tag{3.28}
$$

Where λ is the expected error margin.

For being within the expected error margin, it offers a higher positive reward value; for exceeding the expected error margin, it offers a very low positive reward value. As a result, the learning agent will be encouraged to stay within the expected error margin. The reward function is presented in continuous form by Equation 3.29. It primarily serves as an action penalty reward for the learning agent to reduce

the DRL agent's control effort.

$$\text{Reward}, r = -0.01|u| \tag{3.29}$$

Here, u is the control effort or action output of the proposed DRL agent.

The proposed DRL agent controller employs both reward functions (Equations 3.28 and 3.29) in a hybrid form. The agent attempts to maximize the reward by lowering the output voltage error signal of the proposed CLLL converter.

Actor and Critics Neural Networks   Utilizing actor representation, the TD3-based DRL agent determines which action to execute in response to observations. To develop the actor, a DNN with observation input and action output was built. The actor DNN architecture is portrayed in Figure 3.15. The network has three layers: a feature input layer, a fully connected layer, and a tanh layer. The TD3-

Figure 3.15: TD3 actor DNN architecture.

based DRL agent utilizes two critic value-function representations to approximate the long-term reward given observations and actions. To develop the two critics, a DNN with two inputs, observation and action, and one output has been created. The critics' DNN architecture is illustrated in Figure 3.16.
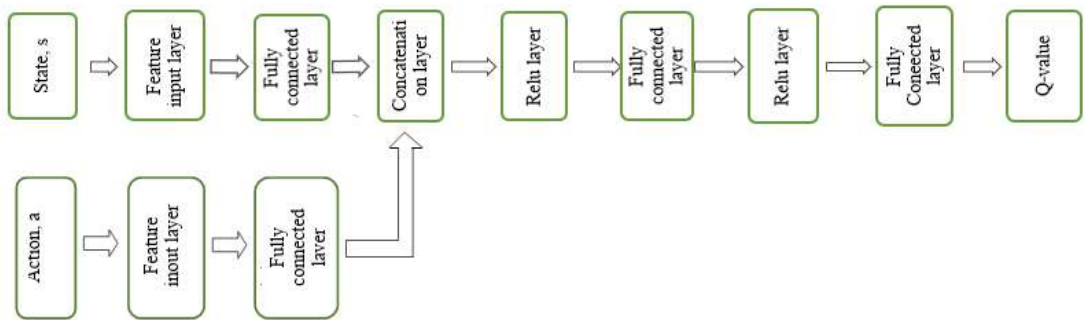
Figure 3.16: TD3 critics DNN architecture.

TD3 Agent hyper-parameters   The hyper-parameters for TD3-based DRL agents are listed in Table 3.2.

Table 3.2: TD3-based DRL agent Hyper-parameters

Hyper-parameters	Settings
Actor learning rate	0.001
Critic learning rate	0.0001
Gradient threshold	1
Gradient threshold method	L2 norm
L2 Regularization factor	0.0001
Optimization algorithm	Adam
Exploration Model	Gaussian action noise
Initial value of noise standard deviation	$\sqrt{0.1}$
Decay rate of the noise standard deviation	0
Target policy smooth model	Gaussian action noise
Policy update frequency, d	2
Target smoothing factor. τ	0.005
Target update frequency	2
Random experience mini-batch size	128
Experience buffer size	1000000
Discount factor, γ	0.995

TD3 Agent Training   The TD3 agent has been trained for up to 1000 episodes, each of which lasts a highest of 3000-time steps. Figure 3.17 depicts the DRL agent learning curves based on TD3 for the last 300 episodes.
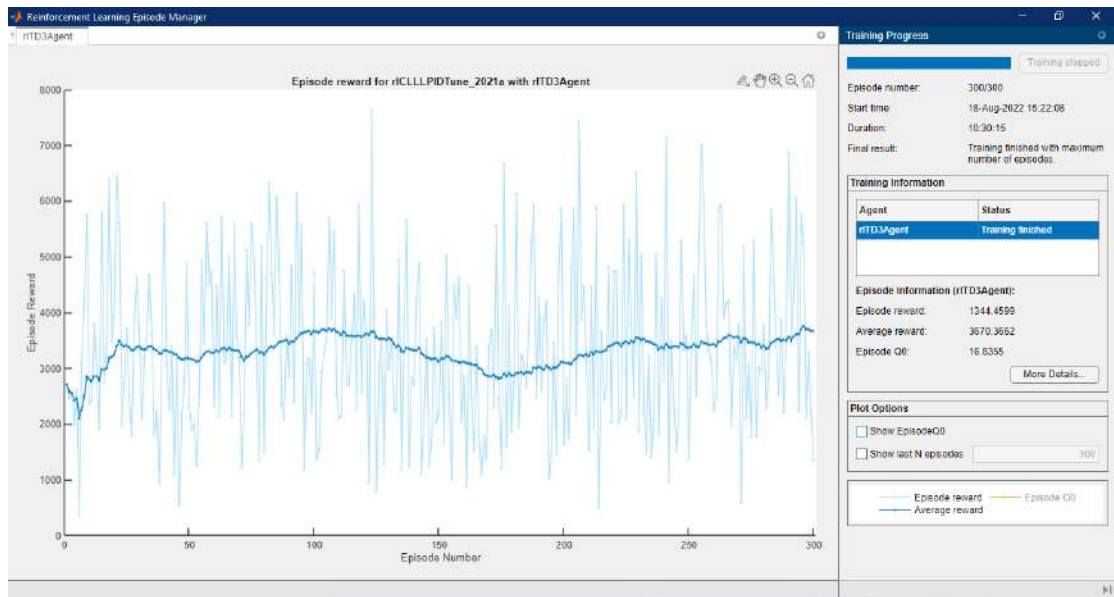
Figure 3.17: TD3-based DRL agent learning curves.

3.2.6.4   Validation of Trained TD3 Agent-Based DRL Controller

The trained TD3-based DRL agent was simulated and compared to conventional PID controllers optimized with PSO and GA. The step response of the three controllers is depicted in Figure 3.18. As shown in Figure 3.18, the PSO and GA-optimized PID controller and proposed TD3-based DRL controller both successfully followed the output voltage reference value. Table 3.3 summarizes the step response performance of these controllers based on various parameters. As can be seen, all of the controllers provide reasonably fast responses. The TD3-based DRL controller responded slightly faster than the PSO and GA-optimized PID controllers in terms of rise time and peak time. The TD3-based DRL controller is an online learning controller in this case, and it can learn and optimize its performance without requiring exact modeling of the proposed DC-DC converter. The PSO and GA-optimized PID controller, on the other hand, is an offline learning controller that requires human assistance to optimize its parameters. It also necessitates the precise modeling of the proposed DC-DC converter. As a result, the proposed TD3-based DRL controller can be effective for developing an intelligent controller for power electronics converters.
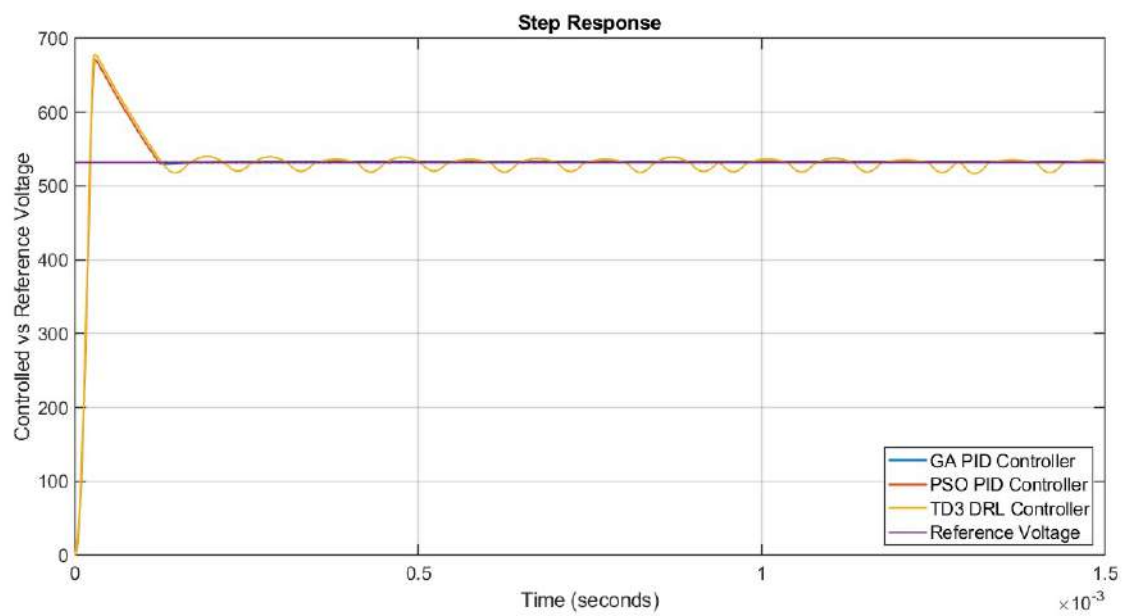
Figure 3.18: Comparison of TD3-based DRL agent step response performance with PSO and GA-optimized PID controllers .

Table 3.3: Step response analysis of TD3-based DRL, GA, and PSO-optimized PID controllers

	GA PID	PSO PID	TD3 DRL
Rise Time (s)	1.4511e-05	1.4520e-05	1.4498e-05
Transient Time (s)	0.0001	0.0001	0.0014
Settling Time (s)	0.0001	0.0001	0.0014
Settling Min (V)	490.5009	490.5009	489.6007
Settling Max (V)	671.1536	671.1536	678.7318
Overshoot (%)	25.7702	25.6524	27.1111
Undershoot (%)	0	0	0
Peak (V)	671.1536	671.1536	678.7318
Peak Time (V)	2.9500e-05	2.9500e-05	2.9000e-05

Chapter 4

Results and Discussions

This chapter outlines the performance of the proposed CLLL converter in both forward and reverse power flow directions with various switching devices based on Si, SiC, and GaN. Conduction loss, switching loss, and junction temperature data for various switching devices were obtained from several manufacturers' websites for realistic simulations. A comparative analysis of these switching devices has been presented to evaluate their performance. A comparison with other recent works is also presented.

4.1 Performance Analysis

To validate the proposed system, simulations using the PLECS Standalone software and MATLAB/Simulink were performed. Figure 4.1 depicts the peak efficiency curves of the proposed CLLL converter using GaN E-HEMT devices under varying load conditions for both G2V and V2G modes. The proposed CLLL converter has a higher efficiency in the charging or G2V mode than in the discharging or V2G mode. In both charging and discharging modes, the proposed converter has good efficiency over a wide load range. Figure 4.2 depicts the peak efficiency, output voltage, and output current vs switching frequency for the proposed converter in both G2V and V2G modes. The peak efficiency was achieved at 1 MHz switching frequency since it is the resonant frequency and accomplishes ZVS turn-on at this frequency. That is why it has the highest efficiency at this frequency. The peak efficiency of the converter began to drop below or above this switching frequency. Because of the same reason, output voltage and output current are at their peak at 1 MHz frequency and begin to decline below or above that level.
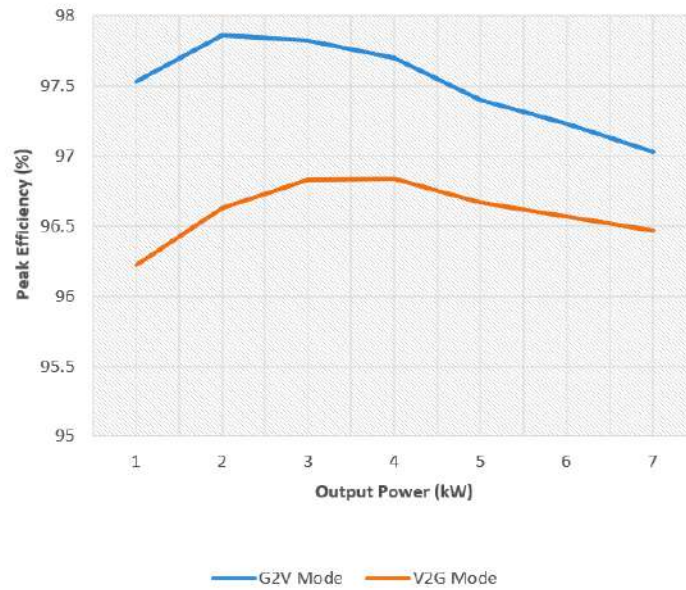
Figure 4.1: Efficiency curves of CLLL Converter utilizing GaN Devices under varying load conditions.

Utilizing automotive standard switching devices built with GaN, SiC, and Si, the performance of the proposed converter was also assessed. PLECS device models, including turn-on loss, turn-off loss, conduction loss, and thermal impedance data, were obtained from various manufacturers' datasheets for practical loss and efficiency calculations. The subsections that follow describe the performance of these devices using this converter.

4.1.1 E-mode GaN HEMT-Based CLLL Converter from GaN Systems Inc.

In this work, a GaN switching device made by GaN Systems Inc., the GS-065-150-1-D2, has been used. The GS-065-150-1-D2 is a $650V, 150A$, and $10m\Omega$ on-resistance enhancement-mode GaN-on-silicon power transistor. It offers zero reverse recovery loss and an extremely high switching frequency ($> 10MHz$). In charging mode, the converter's simulated waveforms are shown in Figure 4.3. It is clear that the switches turn on ZVS. The ripple in the output voltage is almost zero. The circuit yields comparable outcomes in discharging mode.
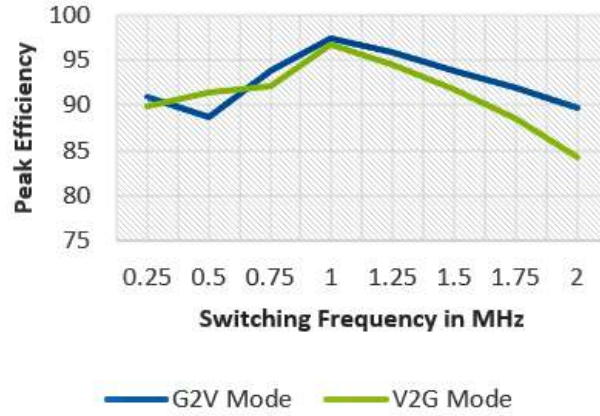
(a) Peak efficiency versus operating switching frequency.
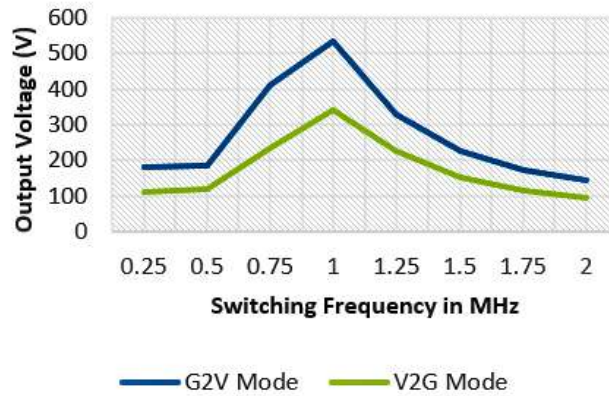
(b) Output voltage versus operating switching frequency.
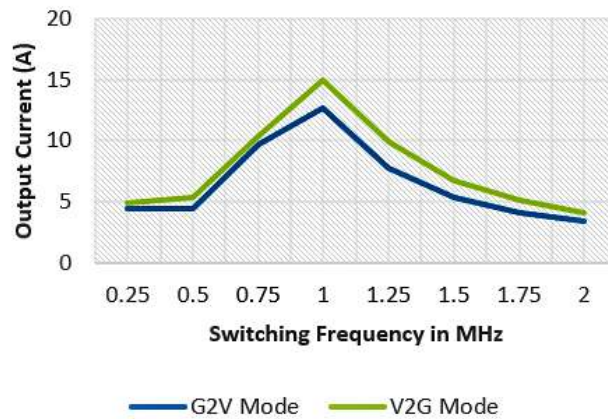
(c) Output current versus operating switching frequency.

Figure 4.2: Peak efficiency, output voltage, and output current versus operating switching frequency for converter operating in the G2V and V2G mode.
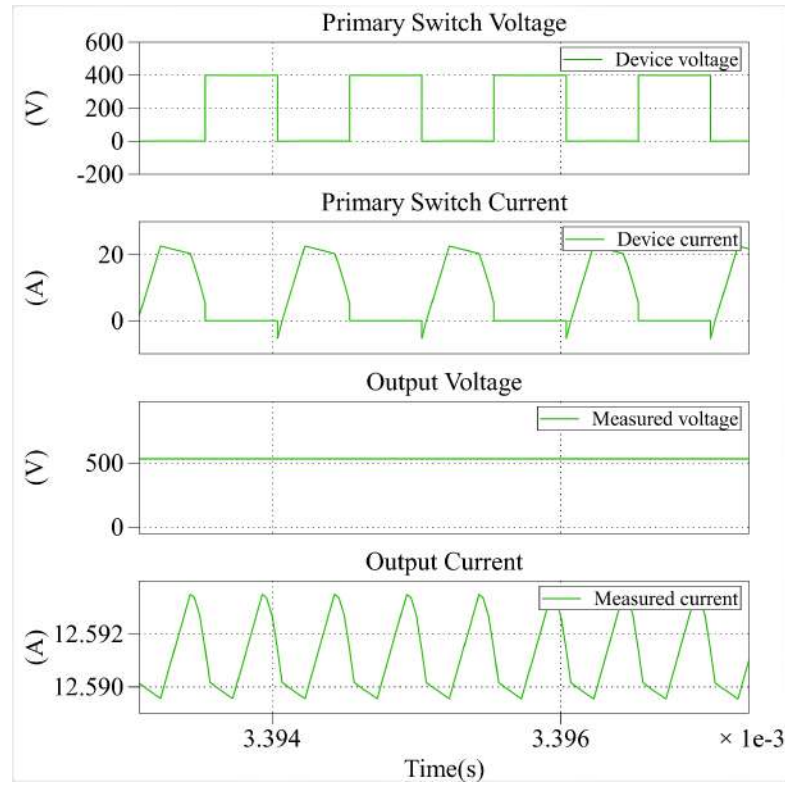
Figure 4.3: E-mode GaN HEMT enabled converter waveforms.

4.1.2 E-mode Planar SiC MOSFET-Based CLLL Converter from Cree Inc.

For this work, the SiC switching device was an n-channel enhancement planar MOSFET with the model number C3M0060065D from Cree Inc. This $650V, 29A$ SiC MOSFET has a fast intrinsic diode with a small reverse recovery (Qrr), fast switching with small capacitances, and high blocking voltage with low on-resistance ($60m\Omega$). Figure 4.4 displays the simulated waveforms for this SiC device's charging mode. The waveforms show the ZVS of the switching device. In comparison to the prior GaN device, the output voltage and current both are marginally lower. Like the GaN device, the output voltage ripple is almost zero. The converter's discharging mode results in waveshapes similar to those.

4.1.3 Trench Structure SiC MOSFET-Based CLLL Converter from ROHM Semiconductor

A trench gate SiC MOSFET with a $650V, 39A$, and $60m\Omega$ on-resistance that is designed for high-efficiency server power supplies, renewable energy systems, and EV chargers is the SCT3060AR from ROHM Semiconductors. The first company
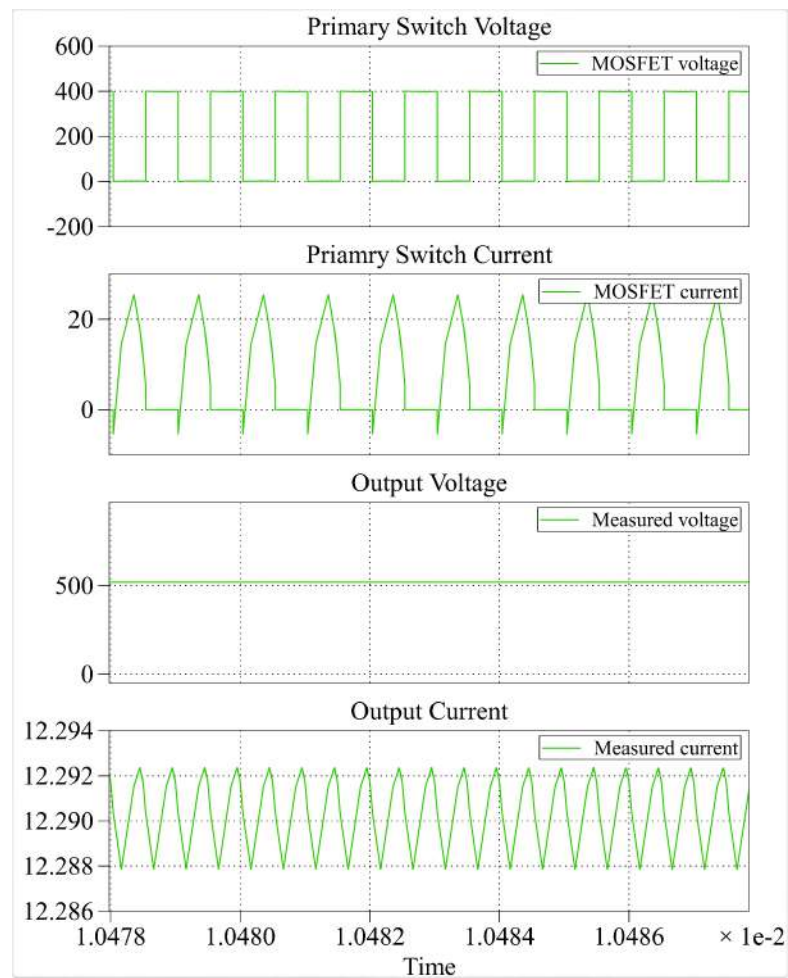
Figure 4.4: Waveforms of the proposed converter with Planar SiC device.

to mass-produce trench-type MOSFETs, which increase efficiency while consuming less power than traditional SiC MOSFETs, was ROHM, a SiC technology pioneer and market leader. The performance of the converter with this device in charging mode is shown in Figure 4.5. It is obvious from the waveforms that this device also displays a ZVS turn-on. In comparison to the previous planar SiC device, the output voltage and current are higher. The Trench SiC device performs better than the previous planar SiC device as a result. Additionally, this device's output voltage and current closely resemble those of the previous GaN device. Similar outcomes are produced by the converter in discharging mode.
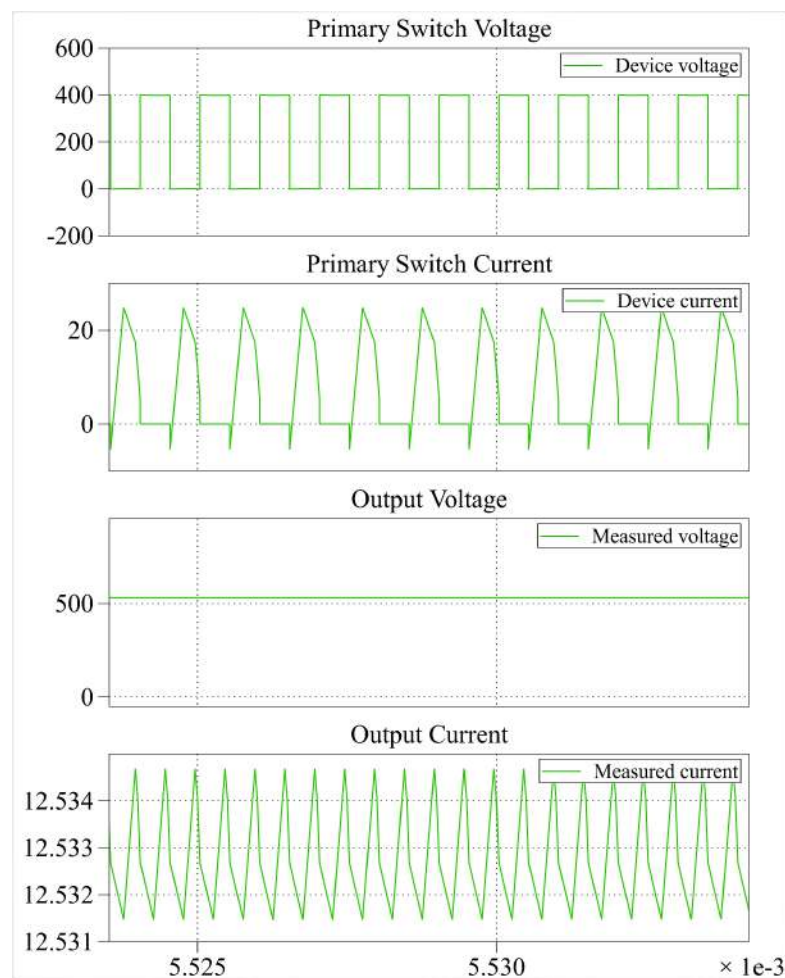
Figure 4.5: Waveforms of the converter with Trench SiC device.

4.1.4 Si Power Transistor-Based CLLL Converter from Infineon Technologies

The SPP20N60C3 Si power transistor from Infineon Technologies has a voltage rating of $650V$, a current rating of $20.7A$, and an on-resistance of $190m\Omega$. This

device has better transconductance, a higher peak current capability, and a very low gate charge. When using this device in charging mode, the performance of the designed converter is shown in Figure 4.6. The output voltage has almost no ripple. The switching device offers a ZVS turn-on in this instance as well. The converter's performance is similar in discharging mode.
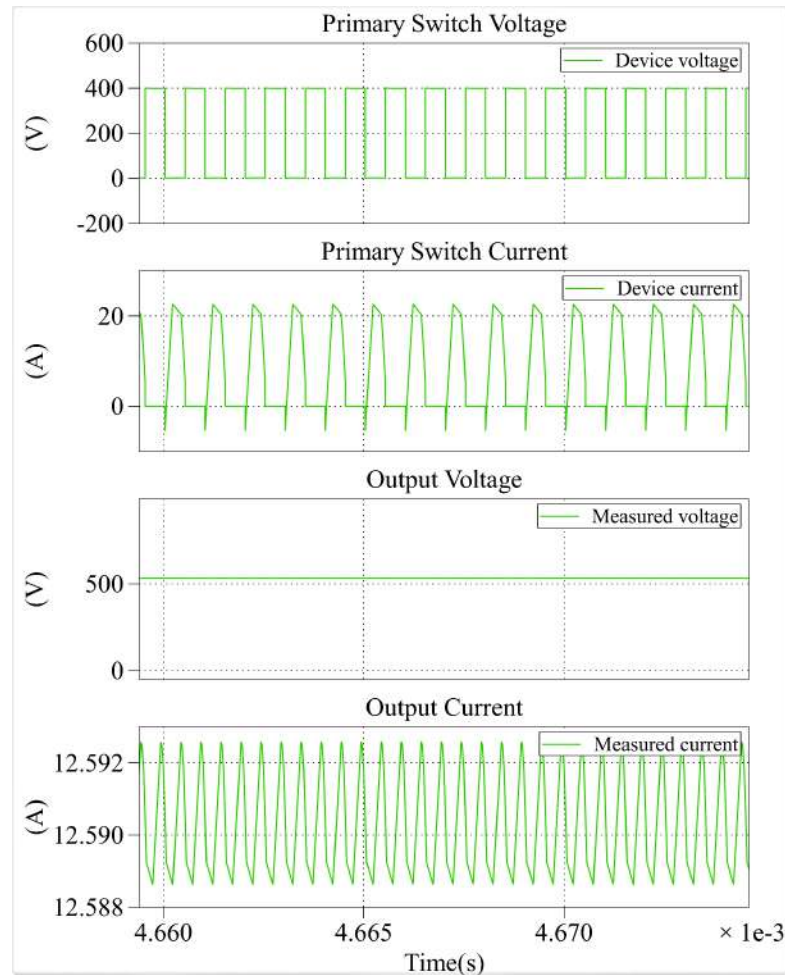
Figure 4.6: Waveforms for the Si Power Transistor based Converter.

4.1.5   Field Stop Trench Si IGBT-Based CLLL Converter from ROHM Semiconductor

The RGW60TS65DHR from ROHM Semiconductor is a 650V 30A Si field stop trench IGBT. This device has a fast recovery diode (FRD) built in for reverse conduction and a low switching loss. The converter's operation with the device in charging mode is shown in Figure 4.7. The output voltage is also free from a ripple in this instance. It guarantees that ZVS is activated as well. The converter functions similarly when discharging.
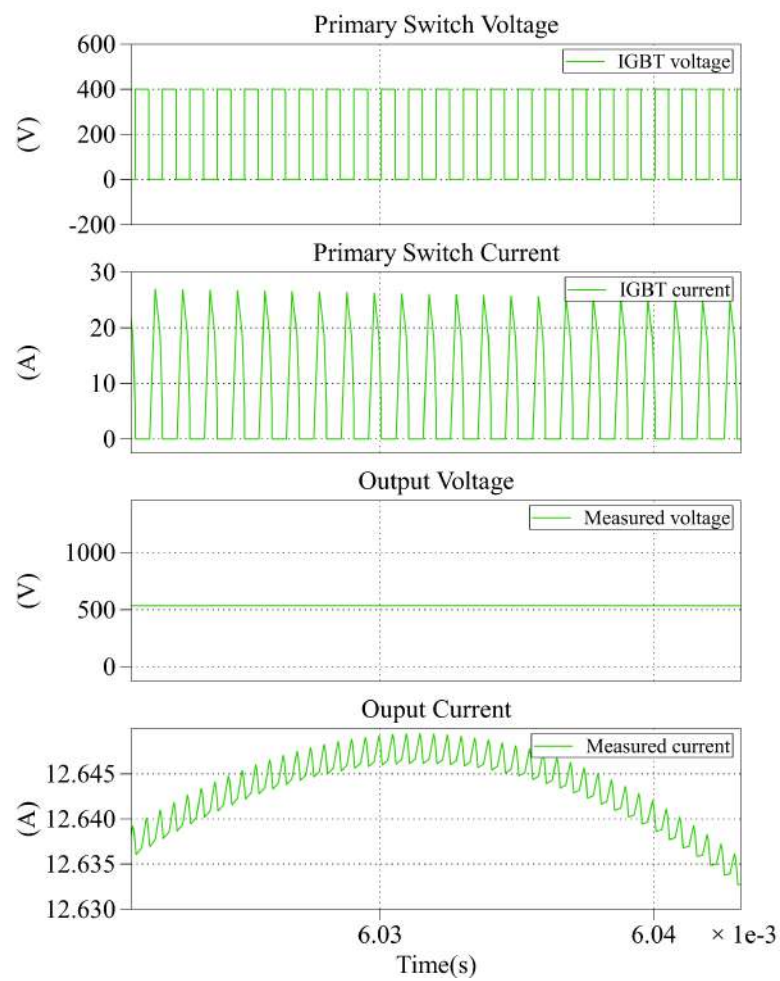
Figure 4.7: Waveforms of the Si IGBT-based converter.

4.2 Comparative Analysis

The loss comparison of the proposed converter in terms of total conduction loss and total switching loss across the primary and secondary switches using the GaN, SiC, and Si-based switching devices is shown in Table 4.1. According to Table 4.1, the GaN System's E-mode GaN HEMT switch outperformed the other SiC and Si-based switching devices in terms of total switching loss across the primary and secondary switches. However, while ROHM's Field Stop Trench Si IGBT performed better than the other GaN, SiC, and Si-based switching devices in terms of total conduction loss, it performed the worst in terms of total switching loss, which is equal to $305.64W$. So, when we consider the two losses of the switches, we can clearly see that the GaN System's E-mode GaN HEMT is the best switching device because its total conduction and switching loss sums to $176.64W$ ($167.79W + 8.85W = 176.64W$), which is significantly lower than the other switching devices. As a result, among the SiC, GaN, and Si-based semiconductor switching devices, E-mode GaN HEMT made by GaN Systems Inc. is the best choice as a switching device for the proposed CLLL converter.

Table 4.1: Loss comparison of the proposed converter

Utilized Switching Device	Total Conduction Loss (W)	Total Switching Loss (W)
E-mode GaN HEMT by GaN Systems Inc.	167.79	8.85
E-mode Planar SiC MOSFET by Cree Inc.	182.82	61.88
Trench Structure SiC MOSFET by ROHM Semiconductor	124.98	121.55
Si Power Transistor by Infineon	158.40	58.70
Field Stop Trench Si IGBT by ROHM Semiconductor	73.40	305.64

The overall effectiveness of the proposed CLLL converter using various switching devices is summarized in Figure 4.8. The designed CLLL converter, which uses a GaN E-mode HEMT as a switching device, has the highest G2V efficiency (97.4%), as shown in Figure 4.8a. GaN devices perform better than SiC and Si MOSFET-based designs, but Si IGBT-based designs perform the worst. According to Figure 4.8b, the situation in charging mode is comparable to that in discharging mode. When different switching devices are used, the designed converter's output current is shown in Figure 4.8c. The lowest and highest output currents were attained by Cree Inc.'s SiC and ROHM Semiconductor's IGBT, respectively. To sum up, an optimized converter solution can be provided by GaN-based switches made by GaN Systems Inc. Moreover, as shown in Table 4.2, in terms of highest G2V efficiency, highest V2G efficiency, and peak output power, this converter outperforms the GaN-based CLLLC resonant dc-dc converter proposed in [7], GaN-based CLLC resonant dc-dc converter proposed in [50], the GaN-based multi-CLLC res-
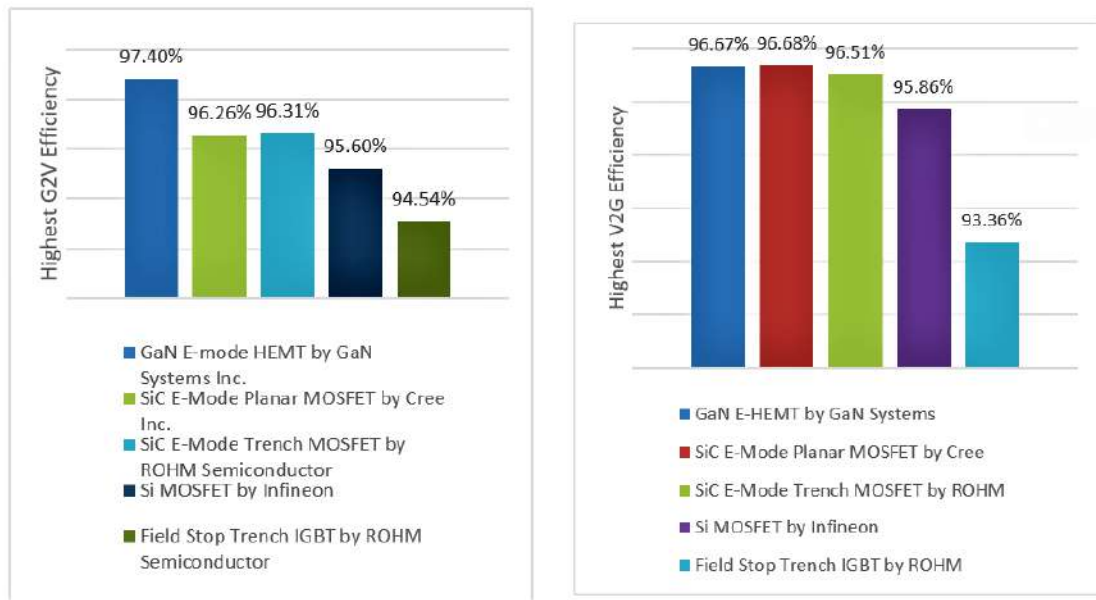
(a) Highest G2V Efficiency.

(b) Highest V2G Efficiency.
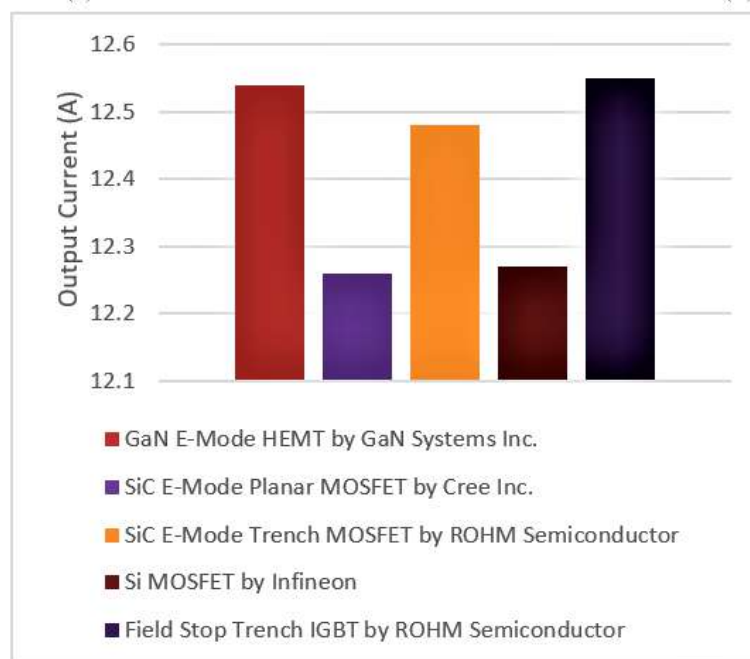
(c) Output Current.

Figure 4.8: Comparison of (a) Highest G2V Efficiency, (b) Highest V2G Efficiency, and (c) Output Current.

onant dc-dc converter proposed in [51], and the GaN-based asymmetric CLLC resonant dc-dc converter suggested in [52]. The highest G2V efficiency (97.4%) and highest V2G efficiency (96.67%) of the suggested converter are both mostly higher than those of the findings presented in [7, 50–52]. The designed converter ensures a high switching frequency ($1MHz$), which is higher than that of [50, 52] and leads to high efficiency and high compactness. To minimize the converter's size and cost, a lower number of resonant elements were chosen for the converter design. In comparison to the proposed converter, [7, 50, 51] utilized a higher number of resonant elements. Additionally, in the resonant elements of the proposed converter, without the capacitance, the two resonant inductances can be integrated with the HF transformer's leakage inductances. Therefore, the proposed converter can result in a more compact design than the converter presented in [7, 50–52]. The GaN-based switching devices were used in all of the converter structures. Only the structure of the resonant converter differs. Moreover, an optimized PID controller is proposed in the designed CLLL converter. Therefore, it is possible to infer that the proposed isolated bidirectional CLLL resonant converter structure is superior to those discussed in [7, 50–52].

Table 4.2: Performance comparison with existing topologies

Criteria	[7]	[50]	[51]	[52]	This work
Max $V_{bus}(V)$	465	540	400	400	610
Switch Technology	GaN	GaN	GaN	GaN	GaN
Switching Frequency (MHz)	1	0.391	1	0.5	1
Resonant Elements	5	5	8	4	4
Highest G2V Efficiency (%)	97.2	95.2	92.2	97.02	97.4
Highest V2G Efficiency (%)	97	95.7	92	95.96	96.67

4.3 Publication

A recent issue of the journal *"International Transactions on Electrical Energy Systems"* [IF: 2.639] published some of the work from this thesis [53].

Chapter 5

Conclusions and Future Work

The key findings and contributions of the thesis are summarized in this chapter along with recommendations for further research.

5.1   Conclusions

This thesis describes the detailed design process for an improved isolated bidirectional resonant converter that uses a CLLL resonant structure. In comparison to the conventional isolated bidirectional CLLLC resonant converter, this resonant converter provides better performance and a more compact design. The converter's input and output voltage ranges are $400 - 460\,V$ DC and $530 - 610\,V$ DC, respectively, at a switching frequency of $1\,MHz$, and it has been developed and tested with a $5 - kW$ rated power. This converter makes it possible to transfer power in both directions while also operating at high frequencies and high efficiency. The switching loss in this MHz scenario is significantly reduced by this CLLL converter architecture, which guarantees soft switching of both primary and secondary semiconductor switches. The optimal PID controller was designed using PSO and GA-based algorithms. This work additionally suggests and analyzes a model-free intelligent DRL controller based on the TD3 algorithm. A comparison was conducted between the DRL controller, the PSO, and the GA-optimized PID controller. For designing an intelligent controller for DC-DC converters, the designed DRL controller could be effective. The proposed converter is in-depth examined in this paper, along with a comparison of the semiconductor switching devices that can be used with it. Due to their low switching loss and zero reverse recovery loss, the proposed CLLL converter employing GaN-based Switching de-

vices from GaN Systems Inc. offers the highest efficiency of any switching device currently on the market. The least efficient designs are those based on Si, followed by SiC-based designs. This GaN-based CLLL converter has peak efficiencies of 97.40 percent for charging and 96.67 percent for discharging at full load. The size of the passive resonant components is also small due to the converter's high frequency ($1\,MHz$) operation. As a result, this proposed converter can thus achieve a high power density. Therefore, this isolated bidirectional CLLL resonant dc-dc converter based on the GaN switching device could be very effective for the EV onboard charger systems due to its high performance and compact design.

5.2 Future Work

In the future, a complete EV battery charger hardware prototype based on the proposed DC-DC converter will be developed, and a comparison of experimental and simulated results will be conducted.

References

[1] R. Irle, "EV-Volumes - The Electric Vehicle World Sales Database," 2022. [Online]. Available: https://www.ev-volumes.com/

[2] Omazaki Group, "Types of Electric Cars and Working Principles — Omazaki Group." [Online]. Available: https://www.omazaki.co.id/en/types-of-electric-cars-and-working-principles/

[3] S. in practice, "Travel — Sustainability in Practice." [Online]. Available: https://sustainability-in-practice.org.uk/three-to-two-planet-living/travel/

[4] D. T. Hoang, P. Wang, D. Niyato, and E. Hossain, "Charging and discharging of plug-in electric vehicles (PEVs) in vehicle-to-grid (V2G) systems: A cyber insurance-based model," *IEEE Access*, vol. 5, pp. 732–754, 2017.

[5] M. D. Galus, M. G. Vayá, T. Krause, and G. Andersson, "The role of electric vehicles in smart grids," *Wiley Interdiscip. Rev. Energy Environ.*, vol. 2, no. 4, pp. 384–400, jul 2013. [Online]. Available: https://wires.onlinelibrary.wiley.com/doi/10.1002/wene.56

[6] L. Tarisciotti, A. Costabeber, L. Chen, A. Walker, and M. Galea, "Current-Fed Isolated DC/DC Converter for Future Aerospace Microgrids," *IEEE Trans. Ind. Appl.*, vol. 55, no. 3, pp. 2823–2832, 2019.

[7] M. T. Shahed and A. B. M. H.-U. Rashid, "Wide Bandgap Semiconductor Based High Performance Bidirectional Resonant Converter for Electric Vehicle Application," in *2022 Int. Conf. Adv. Electr. Electron. Eng.*, feb 2022, pp. 1–6.

[8] Z. Lv, X. Yan, Y. Fang, and L. Sun, "Mode analysis and optimum design of bidirectional CLLC resonant converter for high-frequency isolation of DC distribution systems," *2015 IEEE Energy Convers. Congr. Expo. ECCE 2015*, pp. 1513–1520, 2015.

[9] Z. Liu, F. C. Lee, Q. Li, and Y. Yang, "Design of GaN-Based MHz Totem-Pole PFC Rectifier," *IEEE J. Emerg. Sel. Top. Power Electron.*, vol. 4, no. 3, pp. 799–807, 2016.

[10] S. Zong, G. Fan, and X. Yang, "Double Voltage Rectification Modulation for Bidirectional DC/DC Resonant Converters for Wide Voltage Range Operation," *IEEE Trans. Power Electron.*, vol. 34, no. 7, pp. 6510–6521, 2019.

[11] Y. Chu, A. Kumar, and Y. Ramadass, "Common-Mode EMI cancellation in full-bridge based isolated DC-DC Converters," *Conf. Proc. - IEEE Appl. Power Electron. Conf. Expo. - APEC*, pp. 284–291, 2021.

[12] J. Millan, P. Godignon, X. Perpina, A. Perez-Tomas, and J. Rebollo, "A survey of wide bandgap power semiconductor devices," *IEEE Trans. Power Electron.*, vol. 29, no. 5, pp. 2155–2163, 2014.

[13] Deltrix Chargers, "EV Charging Modes — Deltrix Chargers." [Online]. Available: https://deltrixchargers.com/about-emobility/charging-modes/

[14] G. Rajendran, C. A. Vaithilingam, N. Misron, K. Naidu, and M. R. Ahmed, "A comprehensive review on system architecture and international standards for electric vehicle charging stations," *J. Energy Storage*, vol. 42, p. 103099, oct 2021.

[15] A. A. Mohamed, A. A. Shaier, H. Metwally, and S. I. Selem, "A comprehensive overview of inductive pad in electric vehicles stationary charging," *Appl. Energy*, vol. 262, p. 114584, mar 2020.

[16] Y. Feng and X. Lu, "Construction Planning and Operation of Battery Swapping Stations for Electric Vehicles: A Literature Review," *Energies 2021, Vol. 14, Page 8202*, vol. 14, no. 24, p. 8202, dec 2021. [Online]. Available: https://www.mdpi.com/1996-1073/14/24/8202/htm

[17] G. J. Su, "Comparison of Si, SiC, and GaN based Isolation Converters for Onboard Charger Applications," in *2018 IEEE Energy Convers. Congr. Expo. ECCE 2018.* Institute of Electrical and Electronics Engineers Inc., dec 2018, pp. 1233–1239.

[18] S. G. Jeong, J. M. Kwon, and B. H. Kwon, "High-Efficiency Bridgeless Single-Power-Conversion Battery Charger for Light Electric Vehicles," *IEEE Trans. Ind. Electron.*, vol. 66, no. 1, pp. 215–222, jan 2019.

[19] M. Pahlevaninezhad, P. Das, J. Drobnik, P. K. Jain, and A. Bakhshai, "A ZVS interleaved boost AC/DC converter used in plug-in electric vehicles," *IEEE Trans. Power Electron.*, vol. 27, no. 8, pp. 3513–3529, 2012.

[20] F. Musavi, W. Eberle, and W. G. Dunford, "A high-performance single-phase bridgeless interleaved PFC converter for plug-in hybrid electric vehicle battery chargers," *IEEE Trans. Ind. Appl.*, vol. 47, no. 4, pp. 1833–1843, jul 2011.

[21] B. Hussein, N. Abdi, and A. Massoud, "Development of a three-phase interleaved converter based on SEPIC DC-DC converter operating in discontinuous conduction mode for ultra-fast electric vehicle charging stations," *IET Power Electron.*, vol. 14, no. 11, pp. 1889–1903, aug 2021. [Online]. Available: https://onlinelibrary.wiley.com/doi/full/10.1049/pel2.12157

[22] B. Singh and R. Kushwaha, "A PFC Based EV Battery Charger Using a Bridgeless Isolated SEPIC Converter," *IEEE Trans. Ind. Appl.*, vol. 56, no. 1, pp. 477–487, jan 2020.

[23] Y. Tang, W. Ding, and A. Khaligh, "A bridgeless totem-pole interleaved PFC converter for plug-in electric vehicles," in *Conf. Proc. - IEEE Appl. Power Electron. Conf. Expo. - APEC*, vol. 2016-May. Institute of Electrical and Electronics Engineers Inc., may 2016, pp. 440–445.

[24] D. Das, N. Weise, K. Basu, R. Baranwal, and N. Mohan, "A Bidirectional Soft-Switched DAB-Based Single-Stage Three-Phase AC-DC Converter for V2G Application," *IEEE Trans. Transp. Electrif.*, vol. 5, no. 1, pp. 186–199, mar 2019. [Online]. Available: https://ieeexplore.ieee.org/document/8573905/

[25] S. Gangavarapu and A. K. Rathore, "Three-Phase Buck-Boost Derived PFC Converter for More Electric Aircraft," *IEEE Trans. Power Electron.*, vol. 34, no. 7, pp. 6264–6275, jul 2019.

[26] J. J. Sandoval, S. Essakiappan, and P. Enjeti, "A bidirectional series resonant matrix converter topology for electric vehicle DC fast charging," in *Conf. Proc. - IEEE Appl. Power Electron. Conf. Expo. - APEC*, vol. 2015-May, no. May. Institute of Electrical and Electronics Engineers Inc., may 2015, pp. 3109–3116.

[27] L. Schrittwieser, J. W. Kolar, and T. B. Soeiro, "Novel SWISS Rectifier Modulation Scheme Preventing Input Current Distortions at Sector

Boundaries," *IEEE Trans. Power Electron.*, vol. 32, no. 7, pp. 5771–5785, jul 2017. [Online]. Available: http://ieeexplore.ieee.org/document/7569075/

[28] G. Rajendran, C. A. Vaithilingam, N. Misron, K. Naidu, and M. R. Ahmed, "Voltage oriented controller based vienna rectifier for electric vehicle charging stations," *IEEE Access*, vol. 9, pp. 50 798–50 809, 2021.

[29] R. R. de Melo, F. L. Tofoli, S. Daher, and F. L. M. Antunes, "Interleaved bidirectional DC-DC converter for electric vehicle applications based on multiple energy storage devices," *Electr. Eng.*, vol. 102, no. 4, pp. 2011–2023, dec 2020. [Online]. Available: https://link.springer.com/article/10.1007/s00202-020-01009-3

[30] H. Suryoatmojo, M. Ridwan, I. Izzatur Rahman, D. Candra Riawan, and M. Ashari, "Design of bidirectional DC-DC cuk converter for testing characteristics of lead-acid battery," *Przegląd Elektrotechniczny*, vol. R. 96, nr, no. 3, pp. 114–118, 2020.

[31] P. Gayen, P. Roy Chowdhury, and P. Dhara, "An improved dynamic performance of bidirectional SEPIC-Zeta converter based battery energy storage system using adaptive sliding mode control technique," *Electr. Power Syst. Res.*, vol. 160, pp. 348–361, jul 2018. [Online]. Available: https://linkinghub.elsevier.com/retrieve/pii/S0378779618300889

[32] Y. Zhang, W. Zhang, F. Gao, S. Gao, and D. J. Rogers, "A Switched-Capacitor Interleaved Bidirectional Converter with Wide Voltage-Gain Range for Super Capacitors in EVs," *IEEE Trans. Power Electron.*, vol. 35, no. 2, pp. 1536–1547, feb 2020.

[33] R. Rahimi, S. Habibi, P. Shamsi, and M. Ferdowsi, "An Interleaved High Step-Up DC-DC Converter Based on Combination of Coupled Inductor and Built-in Transformer for Photovoltaic-Grid Electric Vehicle DC Fast Charging Systems," *2021 IEEE Texas Power Energy Conf. TPEC 2021*, feb 2021.

[34] Y. Huangfu, R. Ma, B. Zhao, Z. Liang, Y. Ma, A. Wang, D. Zhao, H. Li, and R. Ma, "A Novel Robust Smooth Control of Input Parallel Output Series Quasi-Z-Source DC-DC Converter for Fuel Cell Electrical Vehicle Applications," *IEEE Trans. Ind. Appl.*, vol. 57, no. 4, pp. 4207–4221, jul 2021.

[35] T. Bhattacharya, L. Umanand, V. S. Giri, and K. Mathew, "Multiphase Bidirectional Flyback Converter Topology for Hybrid Electric Vehicles," *IEEE Trans. Ind. Electron.*, vol. 56, no. 1, pp. 78–84, 2009.

[36] P. K. Joseph and E. Devaraj, "Design of hybrid forward boost converter for renewable energy powered electric vehicle charging applications," *IET Power Electron.*, vol. 12, no. 8, pp. 2015–2021, jul 2019. [Online]. Available: https://onlinelibrary.wiley.com/doi/abs/10.1049/iet-pel.2019.0151

[37] J. W. Lim, J. Hassan, and M. Kim, "Bidirectional Soft Switching Push-Pull Resonant Converter over Wide Range of Battery Voltages," *IEEE Trans. Power Electron.*, vol. 36, no. 11, pp. 12 251–12 267, nov 2021.

[38] M. M. Savrun and A. Atay, "Multiport bidirectional DC-DC converter for PV powered electric vehicle equipped with battery and supercapacitor," *IET Power Electron.*, vol. 13, no. 17, pp. 3931–3939, dec 2020. [Online]. Available: https://onlinelibrary.wiley.com/doi/full/10.1049/iet-pel.2020.0759

[39] Y. Liang, X. Liu, G. Xu, and S. Yue, "A Dual-Transformer-Based Bidirectional DCâĂŞDC Converter of Using Blocking Capacitor for Wide ZVS Range," *IEEE Access*, vol. 8, pp. 170 568–170 578, 2020. [Online]. Available: https://ieeexplore.ieee.org/document/9194005/

[40] C. Bai, B. Han, B. H. Kwon, and M. Kim, "Highly Efficient Bidirectional Series-Resonant DC/DC Converter over Wide Range of Battery Voltages," *IEEE Trans. Power Electron.*, vol. 35, no. 4, pp. 3636–3650, apr 2020.

[41] S. A. Assadi, H. Matsumoto, M. Moshirvaziri, M. Nasr, M. S. Zaman, and O. Trescases, "Active Saturation Mitigation in High-Density Dual-Active-Bridge DC-DC Converter for On-Board EV Charger Applications," *IEEE Trans. Power Electron.*, vol. 35, no. 4, pp. 4376–4387, apr 2020.

[42] B. Yang, "Topology investigation for front end DC /DC power conversion for distributed power system," Ph.D. dissertation, Virginia Polytechnic Institute and State University, 2003. [Online]. Available: https://vtechworks.lib.vt.edu/handle/10919/28982

[43] J. H. Holland, *Adaptation in natural and artificial systems : an introductory analysis with applications to biology, control, and artificial intelligence.* MIT Press, 1992.

[44] J. Kennedy and R. Eberhart, "Particle swarm optimization," *Proc. ICNN'95 - Int. Conf. Neural Networks*, vol. 4, pp. 1942–1948, 1995. [Online]. Available: http://ieeexplore.ieee.org/document/488968/

[45] T. P. Lillicrap, J. J. Hunt, A. Pritzel, N. Heess, T. Erez, Y. Tassa, D. Silver, and D. Wierstra, "Continuous control with deep reinforcement learning," in *4th Int. Conf. Learn. Represent. ICLR 2016.* International Conference on Learning Representations, ICLR, sep 2015. [Online]. Available: https://arxiv.org/abs/1509.02971v6

[46] S. Fujimoto, H. Van Hoof, and D. Meger, "Addressing Function Approximation Error in Actor-Critic Methods," in *35th Int. Conf. Mach. Learn. ICML 2018*, vol. 4. International Machine Learning Society (IMLS), feb 2018, pp. 2587–2601. [Online]. Available: https://arxiv.org/abs/1802.09477v3

[47] C. Cui, N. Yan, B. Huangfu, T. Yang, and C. Zhang, "Voltage Regulation of DC-DC Buck Converters Feeding CPLs via Deep Reinforcement Learning," *IEEE Trans. Circuits Syst. II Express Briefs*, vol. 69, no. 3, pp. 1777–1781, mar 2022.

[48] M. Gheisarnejad and M. H. Khooban, "IoT-Based DC/DC Deep Learning Power Converter Control: Real-Time Implementation," *IEEE Trans. Power Electron.*, vol. 35, no. 12, pp. 13 621–13 630, dec 2020.

[49] Y. Tang, W. Hu, J. Xiao, Z. Chen, Q. Huang, Z. Chen, and F. Blaabjerg, "Reinforcement Learning Based Efficiency Optimization Scheme for the DAB DC-DC Converter with Triple-Phase-Shift Modulation," *IEEE Trans. Ind. Electron.*, vol. 68, no. 8, pp. 7350–7361, aug 2021.

[50] A. M. Ammar, K. Ali, and D. J. Rogers, "A Bidirectional GaN-Based CLLC Converter for Plug-In Electric Vehicles On-Board Chargers," *IECON Proc. (Industrial Electron. Conf.*, vol. 2020-Octob, pp. 1129–1135, 2020.

[51] Y. F. Wang, B. Chen, Y. Hou, Z. Meng, and Y. Yang, "Analysis and Design of a 1-MHz Bidirectional Multi-CLLC Resonant DC-DC Converter with GaN Devices," *IEEE Trans. Ind. Electron.*, vol. 67, no. 2, pp. 1425–1434, 2020.

[52] Y. Liu, G. Du, X. Wang, and Y. Lei, "Analysis and design of high-efficiency bidirectional GaN-based CLLC resonant converter," *Energies*, vol. 12, no. 20, 2019.

[53] M. T. Shahed and A. B. M. H.-U. Rashid, "An Improved Topology of Isolated Bidirectional Resonant DC-DC Converter Based on Wide Bandgap Transistors for Electric Vehicle Onboard Chargers," *Int. Trans. Electr. Energy Syst.*, vol. 2023, 2023.

Appendix A

Algorithms

Algorithm A.1: Pseudocode of Genetic Algorithm

---
1 Initialize Random Population;
2 Evaluate the population;
3 *Generation = 0*;
4 **while** *the termination criterion is not satisfied* **do**
5   *Generation = Generation + 1*;
6   Select elite individuals with lower fitness scores;
7   Perform crossover with probability crossover;
8   Perform mutation with probability mutation;
9   Evaluate the population;
10 **end**
11 Return the best individual during the evolution;

Algorithm A.2: Pseudocode of PSO Algorithm

---
1 Initialize the size of the particle swarm and other parameters;
2 Randomly Initialize the position and velocity of particles;
3 **while** *the termination criterion is not satisfied* **do**
4   **for** *i = 1 to the number of particles* **do**
5   Calculate the fitness function;
6   Update the personal and global best of each particle;
7   Update the velocity of the particle;
8   Update the position of the particle;
9   **end**
10 **end**
11 Return the position of the best particle;

Algorithm A.3: Pseudocode of Twin Delayed DDPG (TD3) Algorithm

---

1 Initialize critic networks $Q_{\theta_1}, Q_{\theta_2}$, and actor network π_ϕ with random parameters θ_1, θ_2, ϕ;

2 Initialize target networks $\theta_{1'} \leftarrow \theta_1, \theta_{2'} \leftarrow \theta_2, \phi' \leftarrow \phi$;

3 Initialize replay buffer $\mathcal{B}$;

4 for $t = 1$ **to** T **do**

5 $\quad$ Select action with exploration noise $a \sim \pi_\phi(s) + \epsilon, \epsilon \sim \mathcal{N}(0, \sigma)$;

6 $\quad$ Execute action a in the environment;

7 $\quad$ Observe reward r and next state s';

8 $\quad$ Store Transition Tuple (s, a, r, s') in $\mathcal{B}$;

9 $\quad$ Randomly sample mini-batch of N transitions (s, a, r, s') from $\mathcal{B}$;

10 $\quad$ Calculate target actions: $\tilde{a} \leftarrow \pi_\phi(s') + \epsilon, \epsilon \sim \text{clip}(\mathcal{N}(0, \sigma), -c, c)$;

11 $\quad$ Calculate targets: $y \leftarrow r + \gamma \min_{i=1,2} Q_{\theta_{i'}}(s', \tilde{a})$;

12 $\quad$ Update critics $\theta_i \leftarrow \text{argmin}_{\theta_i}$ by minimizing the loss:
$\quad$ $L(\theta_i) = \frac{1}{N} \sum_{j=1}^{N} (y_j - Q_{\theta_i}(s_j, a_j))^2$;

13 $\quad$ **if** t *mod policy delay* d **then**

14 $\quad\quad$ Update the actor policy ϕ by the deterministic policy gradient:
$\quad\quad$ $\nabla_\phi J(\phi) = \frac{1}{N} \sum \nabla_a Q_{\theta_1}(s, a)|_{a=\pi_\phi(s)} \nabla_\phi \pi_\phi(s)$;

15 $\quad\quad$ Update the target networks with a slow-moving update rate, τ:

$$\theta_i' \leftarrow \tau\theta_i + (1 - \tau)\theta_i'(\text{critic}),$$
$$\phi' \leftarrow \tau\phi + (1 - \tau)\phi'(\text{actor});$$

16 $\quad$ **end**

17 end